EXPERIMENTAL AND THEORETICAL INVESTIGATION OF OPTIMAL CONTROL METHODS WITH MODEL REDUCTION

by

George C. Schamel II

Dissertation submitted to the Faculty of the

Virginia Polytechnic Institute and State University

in partial fulfillment of the requirements for the degree of

Doctor of Philosophy

in

Aerospace Engineering

APPROVED:

Raphael T. Haftka

William L. Hallauer, Jr.

Eugene M. Cliff

Frederick H. Lutze

Harry H. Robertshaw

July, 1989

Blacksburg, Virginia

EXPERIMENTAL AND THEORETICAL INVESTIGATION OF OPTIMAL CONTROL METHODS WITH MODEL REDUCTION

by

George C. Schamel II

Raphael T. Haftka

William L. Hallauer, Jr.

Aerospace Engineering

(ABSTRACT)

In this study three types of optimized controllers are developed and tested on two laboratory structures. The two structures represented a progression in complexity and challenge to the controllers. The first structure was simple enough to be accurately modeled so the analytical frequencies and mode shapes agreed with the experimental measurements. The second structure being more complex was more difficult to model so differences between the analytical results and experimental measurements were present. These differences required the application a correction method to the reduced models developed for the second structure. The correction method was shown to work with good results on one reduced model and with poor results on the second reduced model.

Two direct rate feedback control laws and an linear quadratic regulator with state estimation (LQG controller) were designed and implemented on both structures. It was shown that the performance of the LQG controller can be approached with a much simpler direct rate feedback controller with better analytical-experimental agreement. The best analytical-experimental agreement

occurred with the simplest controller applied analytically to the corrected reduced model demonstrating the validity of the correction method as well as giving a strong reason to use simpler controller designs.

Acknowledgements

I am greatly indebted to my committee co-chairmen Raphael T. Haftka and William L. Hallauer, Jr. for their patience and guidance through the course of my graduate studies. Dr. Haftka provided the guiding hand that steered the analytical side of research while Dr. Hallauer provided me with a sound background in experimental research that allowed me to conduct the experiments with only his verbal aid over the telephone.

I would like to thank my committee members Eugene M. Cliff, Frederick H. Lutze, and Harry H. Robertshaw for their consultation and time throughout the years.

I appreaciate the support of NASA Langley Research Center for the grant NAG-1-224 which supported this research.

Thanks are due to the staff of the Aerospace and Ocean Engineering Department particularly the office staff , , and .

I am grateful for the support and friendship of my fellow graduate student in the structures lab.

Finally, I wish to thank my parents and and my wife for their support and encouragement through the years of education.

Table of Contents

List of Illustrations

List of Tables

Chapter 1

Introduction

Active damping of structural vibrations is a subject of growing interest for many areas of engineering applications. Structures are being optimized for minimum weight designs and therefore are becoming more flexible and subject to vibrations which may have a detrimental effect on their performance. The area of engineering toward which this study is directed is the active damping of a large space structure (LSS) disturbed by environmental or maneuver conditions. LSS will be designed for minimum weight to lower the cost of orbiting its structural elements. Additionally, the structure will be extremely lightweight since it will not need to sustain the gravitational loading present on Earth. These factors lead to a structure with low and closely spaced frequencies, and lightly damped modes of vibration. Active damping (control) will be needed to maintain the integrity of overall system performance.

The size and complexity of projected LSS will require a very high order finite element model of the structure. It is extremely difficult or impossible to design and implement control systems directly for high order models. Consequently, control systems are typically designed based on a reduced order model including only the lowest frequency vibration modes and a limited number of physical degrees-of-freedom (DOFs). Many types of model reduction methods have been proposed (see, for example, Refs. 1-9) but not much information on their application to actual structures with active control systems is available.

The accuracy of the finite element model of a real structure also plays an important part in the design and performance of a control system. If the frequencies and mode shapes of the model are not accurate compared to experimental values, the control systems designed will not perform as predicted and may even drive the structure unstable. Therefore system identification techniques are employed to correct the analytical model of the structure with experimental measurements. Several different methods are in use today (e.g. Refs. 10-23), some use only experimental data, (time domain and frequency domain), and some use both experimental measurements and analytical results.

A great number of studies of active vibration control of LSS have been produced in the past. Reference 24 published in 1984 is a survey of this subject and it cites nearly 200 publications. The vast majority of these are purely theoretical investigations, only 13 are experimental in nature. References 25 - 27 are representative of the most significant of these early experimental studies. A form of optimal control using modal states rather than physical states is implemented

in Ref. 25. An important aspect of this work is their use of structure-borne sensors and actuators. Reference 26 describes the construction of a flexible beam laboratory structure and the implementation of various control forms. Optimal estimation and control laws are implemented in Reference 27 on a very complex structure, a three dimensional flexible off-set feed antenna. While these three references represent significant early research in active vibration control, they also represent the relatively uninformative forms of experimental data previously published, consisting primarily of time histories of response with no theoretical correlation.

Since 1984, there have been an increasing number of combined experimental/theoretical investigations. References 28 - 48 are a cross-section of the experimental/theoretical investigations published since 1984. A modal space approach to active damping is investigated in Refs. 28 to 30 with modal reduction and colocated sensors and actuators. References 31 to 33 report efforts at system identification and control of a truss structure. In this research the authors found that it was useless to design high performance control systems for their structure until an extensive system identification process had been performed. References 34 and 35 investigate the possiblity of improving the performance of the control system by making small mass and stiffness changes to a structure. Two new ideas for designing control systems based on direct velocity feedback are applied to different structures in References 36 and 37. Reference 37 also investigates the effects of model reduction and correction on the performance of control laws. (These two papers present some of the results developed in this dissertation.)

Various other control laws and implementation schemes are investigated in References 38 to 48. Control laws are implemented through structural members that can change shape or exert internal forces in References 41 to 43. Experiments that use structure borne sensors and actuators that are not a part of the structure are reported in Refs. 45 to 48.

Many of these publications use system identification techniques or model reduction methods but few of them address the question of "How does the choice of identification or reduction techniques affect the correlation between experiment and theory?". This is the question addressed in this dissertation.

The objective of this research is to investigate two ways of improving the correlation of analytical and experimental data. The first is to determine which of four types of active control of varying complexity is least sensitive to modeling errors. The second is to use a model correction technique on two different reduced models. These control laws are applied to two laboratory structures: a simple beam structure and a more complex hanging grid structure.

Chapter 2 introduces the two structures used and the correlation of the finite element model results with open loop experimental results. The two model reduction methods used in this study are explained in Chapter 3 along with the correction to the reduced models based on experimental results. The control laws are explained and developed in Chapter 4. Chapter 5 discusses the experimental apparatus and procedures used. Analytical and experimental results are presented in Chapter 6 and some concluding remarks are made in Chapter 7.

Chapter 2

Structural Models

In order to evaluate various active control designs, experimentally and analytically, both physical structures and accurate models of these structures are needed. Ideally, the experimental structure would exhibit several of the dynamic characteristics associated with large flexible space structures: very low frequency modes, high modal density, and low inherent damping. A structure in orbit will naturally have several rigid body modes, which are extremely difficult to reproduce within a gravitational field. The vacuum of space is also difficult to reproduce in a small earth-based laboratory. Therefore, a ground-based experiment can only reasonably model the first three characteristics stated: low frequency, high modal density, and low damping.

The two structures used in this study were designed to have those characteristics to some degree. The first structure consisted of a flexible steel beam suspended vertically between the floor and ceiling of the laboratory area. A

horizontal aluminum crosspiece was attached to the vertical beam to provide a pair of modes closely spaced in frequency. The second structure was composed of a flexible aluminum grid suspended from a steel top beam assembly mounted in rotational bearings. Together the two structures presented a reasonable progression of complexity to challenge control applications.

2.1 Beam Cross-Cable Structure

The beam cross-cable structure, which has been the subject of a previous Master's thesis [Ref. 49] and several papers, [Refs. 34,36, and 50] , consisted of an 80-inch long steel beam suspended vertically by four steel cables in tension and a 32-inch horizontal aluminum crosspiece clamped to the steel beam 20-inches up from the bottom of the beam as shown in Figure 1. The vertical steel beam had a uniform rectangular cross section, 2 inches wide by 1/8 inch thick, with the 2 inch dimension in the plane formed by the four 0.09 inch diameter suspension cables. The crosspiece assembly consisted of an aluminum beam 32 inches long, 2 inches wide and 1/8 inch thick with symmetric tip masses. Sectional bending moduli (EI) were experimentally determined (statically and dynamically) for both steel and aluminum beams. The sectional bending modulus for the steel beam was 9060 lb-in^2 and for the aluminum beam it was 2680 lb-in^2 . This structure had three pairs of colocated velocity sensor/force actuators located at the base of the beam, 20 inches up, and 40 inches up from the base of the vertical beam.

2.1.1 Finite Element Model

A two dimensional finite element model was developed for the Beam Cross-Cable structure. The model had eight 10-inch beam elements representing the vertical beam, two string-in-tension elements for the four cables, and a single degree-of-freedom spring-mass model representing the crosspiece. This model also included two one inch rigid inserts to model the increased stiffness caused by the clamp holding the crosspiece to the vertical beam. Figure 2 is a representation of the finite element model showing the string-in-tension elements at the top and bottom of the beam, the vertical beam elements and their associated degrees-of-freedom (DOFs), the spring-mass system modeling the crosspiece with the rigid inserts on the vertical for the clamp, and the coils which are the structure-borne parts of the sensors and actuators. A more complete description of the model may be found in Reference 49.

2.1.2 Experimental/Analytical Results

The Beam Cross-Cable structure was designed to have several low frequency, lightly damped modes below 25 Hz. Additionally, it was to have two modes close in frequency. Experimentally measured and analytically predicted natural frequencies demonstrated the achievement of these goals as well as the accuracy of the finite element model. Table 1 lists the experimental and analytical natural frequencies below 25 Hz and experimental damping ratios for these modes. The

closely space modes are modes 3 and 4 with mode 3 being only 7 percent lower in frequency than mode 4. The agreement between the experimental and analytical frequencies is good with a maximum difference of 2.4 percent in the first mode. Analytical mode shapes are presented in Figure 3. Notice that the major difference between modes 3 and 4 is the relative phase between the end of the crosspiece and the center of the beam. Figure 4 displays experimental and analytical displacement frequency response functions (DFRFs) for excitation at the base of the vertical beam and response 30 inches above the base of the beam. Proportional damping equivalent to the measured open loop inherent damping of the structure was included in the analytical model. The modal damping ratios were obtained experimentally by curve fitting the DFRFs and by measuring vibration decay traces. The shape of the DFRFs is quite similar, but looking at the analytical to experimental peak level ratios (Table 2) reveals large differences in four of the six modes.

2.2 Hanging Grid Structure

The second, more complex structure used in this study was the hanging grid structure, originally designed by Masse (Ref. 51) and later modified and analyzed by Gehling (Ref. 52). A line drawing of the grid structure is shown in Figure 5. This structure is a much more challenging system to model and control than the Beam Cross-Cable structure. The grid is composed of lightweight aluminum

beams 2 x 1/8 inches in cross section bolted tightly at each of the joints. It hangs vertically from a steel top beam assembly with a discontinuous sandwich construction. Large aluminum plates 11/16 inches thick are attached to the ends of the top beam to create a low frequency pendulum mode. The ends of the top beam beyond the aluminum plates are mounted in pillow block bearings to allow nearly frictionless rotation. The flexibility of the aluminum grid provides many low frequency flexible modes and the off-set aluminum plates provide a low frequency nearly rigid body mode.

The structure has both in-plane and out-of-plane modes relative to the plane of the grid, but these two types of modes are decoupled by geometry. Only out-of-plane excitation and response were considered in this study.

Velocity sensors are available at all twelve of the joints on the grid and force actuators are colocated with five of these sensors at joints 1,2,4,5, and 8. Additional motion sensing was made using Bentley-Nevada non-contacting displacement probes. For additional information on the sensors and actuators, see Chapter 5 section 1.

2.2.1 Finite Element Model

The hanging grid structure was modeled in two dimensions with 30 beam finite elements connected at the 22 grid points labeled on Figure 5. The DOFs at each grid point are out-of-plane translation and rotations about the horizontal and

vertical in-plane axes. Translations are restrained at grid points 13 and 22 so the total number of DOFs is 64.

The beam element stiffness and mass matrices used for the aluminum grid are standard, with bending deformation based on Euler-Bernoulli theory with cubic shape functions, and torsional deformation based on linear shape functions (Ref. 53). One exception to this standard approach is that bending shear flexibility is included to account at least roughly for the discontinuous sandwich design of the top beam, evident in Figure 5. Gravity-induced in-plane forces, shear forces, and bending moments have significant influence on the out-of-plane stiffnesses of the thin aluminum grid members. This influence is represented by element geometric stiffness matrices (Ref. 54).

The thick aluminum plates are modeled as being rigid. The product of weight W times eccentricity Y of each plate acts as a pendulous rotational stiffness about the beam assembly axis at the location where the plate joins the beam assembly. This is modeled by the attachment of a grounded rotational spring with stiffness WY at grid points 13 and 22.

2.2.2 Experimental/Analytical Results

The hanging grid structure was intended to have a higher modal density and more pairs of closely spaced frequencies than the Beam Cross-Cable structure. Table 3 presents the first twelve natural frequencies of the hanging grid structure with the associated damping ratios. All twelve of these frequencies are under 10

Hz (a higher modal density than the BCC structure) and two pairs of closely spaced frequencies are in these twelve, modes 4 and 5 and also modes 7 and 8. The agreement between the analytical and experimental frequencies is very good for modes 3 through 12 and only off about 13% for modes 1 and 2. The experimental frequency obtained for mode 1 is about 10% higher than the frequency obtained in a previous study (Ref. 55). This is due in part to the attachment of several small wires to the structure for the control actuators. Damping ratios are generally higher for this structure because of the number of joints in the structure and the larger surface area to provide air friction. The experimental procedure for this testing is described in Chapter 5.

Analytical and experimental mode shapes are presented in Figures 6 through 16 for the first 11 modes of the structure, above each analytical/experimental pair is a plot of the difference between them. The two mode shape plots are drawn assuming a unit maximum deflection and the difference plot is drawn on the same scale. Some differences are present in all modes but the largest are in modes 7 and 8 which are first bending and torsion of the top beam respectively. The bending motion of the top beam is not shown in Figure 12 because no displacement measurements were made along the top beam. Since these are top beam modes, the grid joints are not the best points from which to measure the motion and this may account for some of the discrepancy. Figures 17 to 20 are analytical and experimental Velocity FRFs for the uncontrolled structure. Figure 17 displays the VFRFs for the structure forced at joint 4 and the velocity measured at joint 1. Note the absence of a peak for the second mode in the experimental

VFRF where a noticeable peak is present in the analytical results. This difference may be due to the small amplitude of motion at joint 1 associated with mode 2. As can be seen from Figure 7, the analytical mode shape has larger amplitude at joint 1 than the experimentally measured mode shape. Figure 18 presents experimental and analytical VFRFs for excitation at joint 4 and response at joint 2. In this figure noticeable differences can be seen in mode 2 and 5. Figure 19 is the VFRFs for excitation at joint 4 and response at joint 3. Noticeable differences between the experiment and analysis are present in mode 5. The poor modeling of mode 5 in these two VFRFs may be because this mode has the largest difference of all modes between analytical and experimental mode shapes at the excitation point, joint 4 (see Figs. 6-16). Figure 20 presents the best agreement between analysis and experiment for this model. It displays VFRFs for both excitation and response at joint 4. Some noticeable differences are still present in the first three modes. The damping ratios used in the analytical VFRFs were obtained experimentally through curve fitting the experimental VFRFs and iteratively by attempting to match peak levels for a number of response points. From these VFRFs, it can be seen that frequency and mode shape differences have a noticeable effect on the dynamic behavior of the system.

Table 1. Experimental/Analytical Frequencies and Damping Ratios for the Beam Cross-Cable Structure

Mode	Frequencies (Hz)		Damping Ratios
	Experimental	Analytical	Experimental
1	1.899	1.853	0.004
2	4.771	4.803	0.002
3	8.719	8.799	0.004
4	9.404	9.490	0.002
5	14.71	14.44	0.003
6	22.55	22.73	0.001

Table 2. Analytical/Experimental Open Loop Peak Level Ratios for the Beam Cross-Cable Structure

Mode	Open Loop
1	0.55
2	0.17
3	1.00
4	0.50
5	0.35
6	1.00
Avg. Error	0.41

Table 3. Experimental/Analytical Frequencies and Damping Ratios for the Hanging Grid Structure

Mode	Frequencies (Hz)		Damping Ratio
	Experimental	Analytical	Experimental
1	0.687	0.593	0.043
2	0.949	0.840	0.045
3	1.47	1.45	0.035
4	3.33	3.35	0.010
5	3.64	3.60	0.009
6	5.22	5.14	0.013
7	5.57	5.57	0.004
8	5.78	5.75	0.003
9	6.36	6.22	0.006
10	7.89	8.08	0.006
11	8.39	8.50	0.005
12	9.60	9.60	0.005

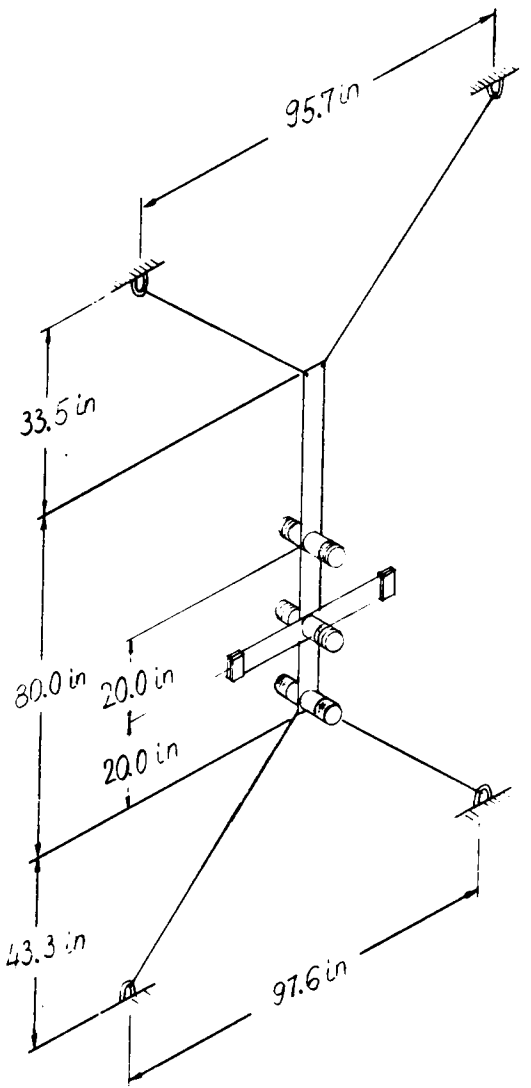

Figure 1. Line Drawing of the Beam Cross-Cable Structure

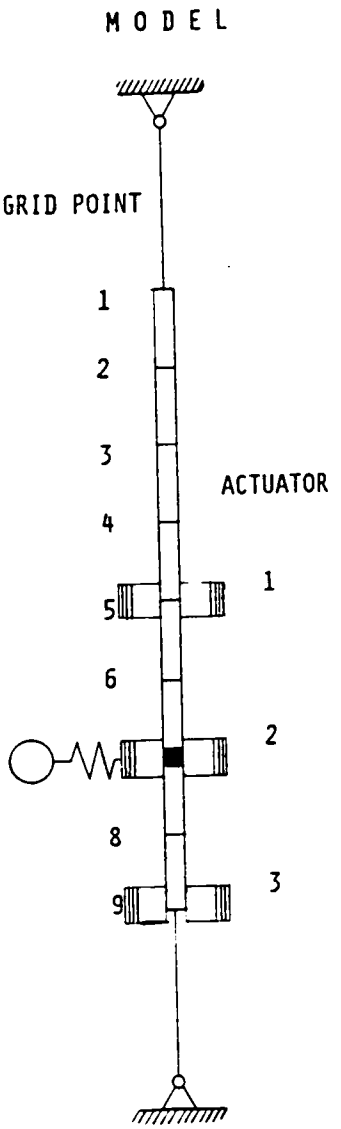

Figure 2. Finite Element Model the Beam Cross-Cable Structure

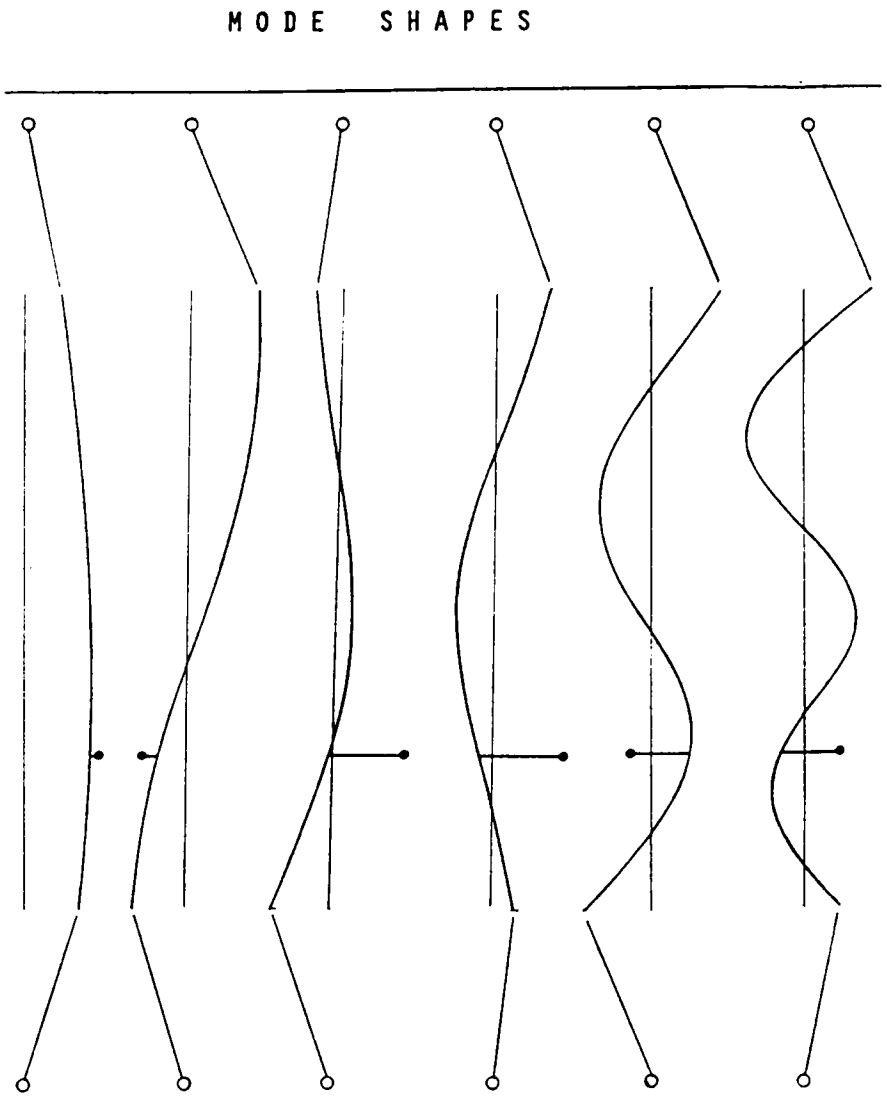

	MODE	1	2	3	4	5	6
FREQ. (Hz)	EXPER.	1.9	4.8	8.7	9.4	14.7	22.5
	THEORY	1.9	4.8	8.8	9.4	14.4	22.7

Figure 3. Analytical Mode Shapes for the Beam Cross-Cable Structure

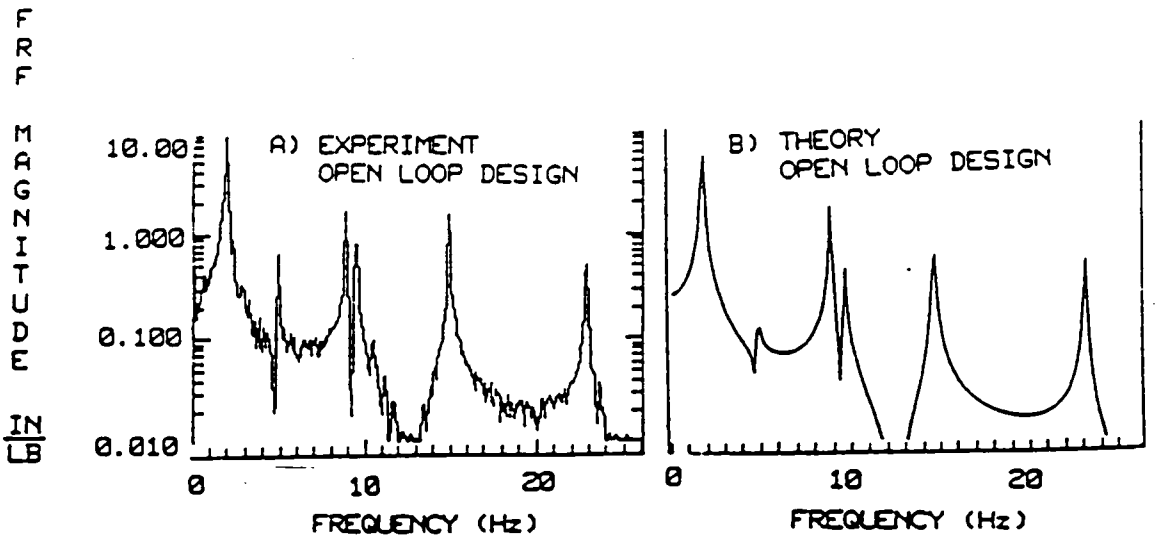

Figure 4. **Analytical/Experimental Displacement Frequency Response Functions of the Beam Cross-Cable Structure: Excitation at base of beam and response 30 inches above.**

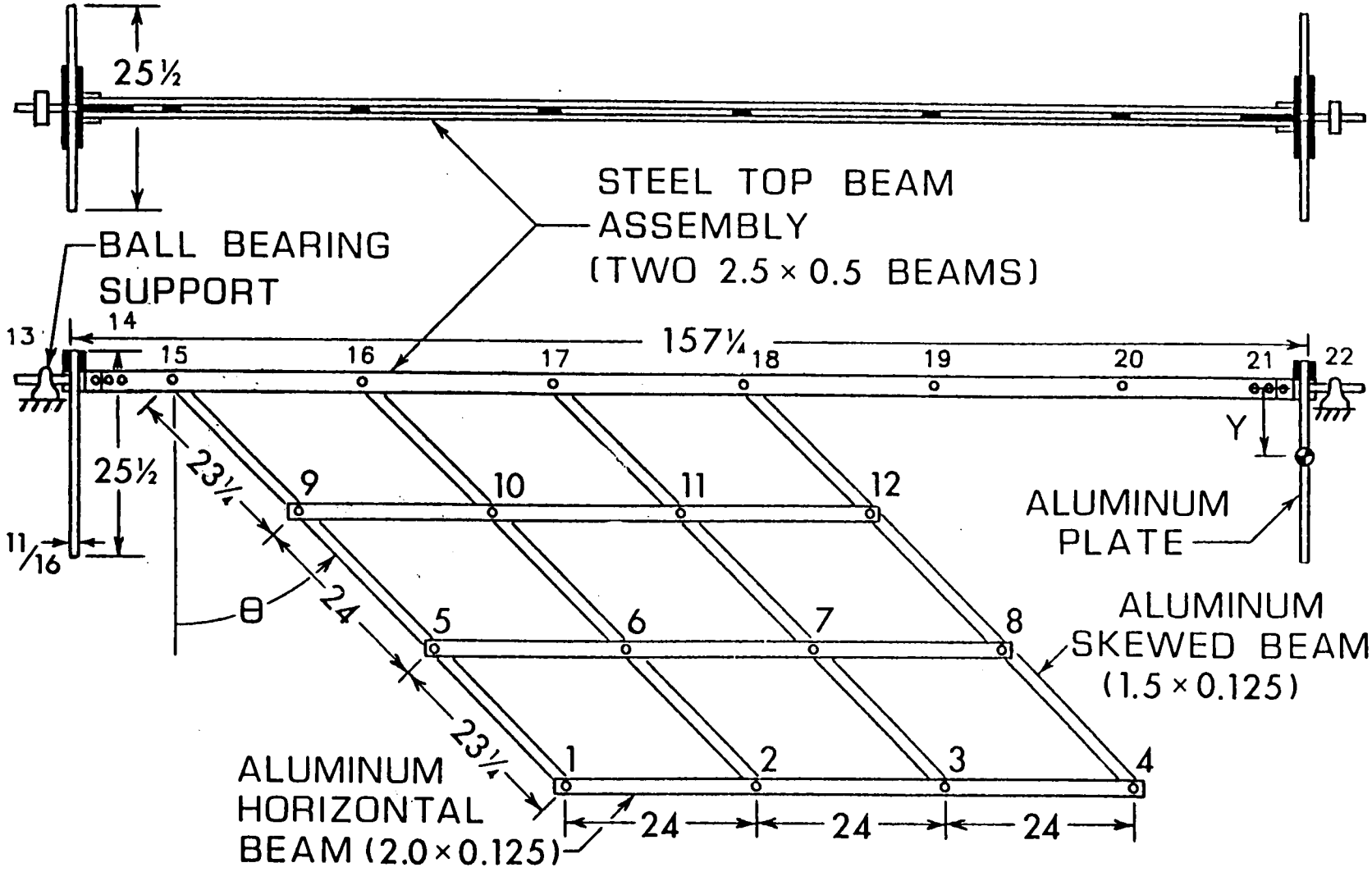

Figure 5. **Line drawing of the laboratory structure with grid points numbered.** (θ = 45 Deg , Y = 9.05 in)

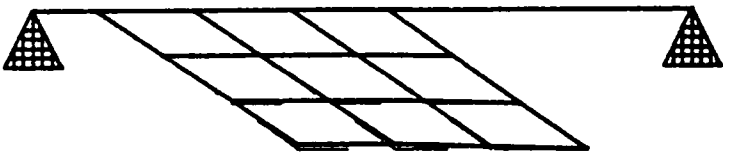

Difference

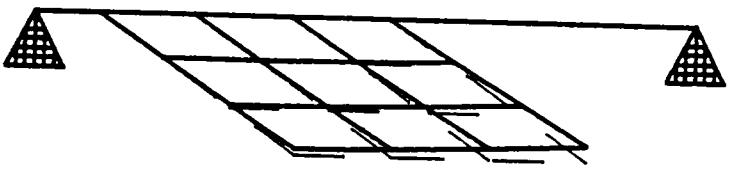

Analytical

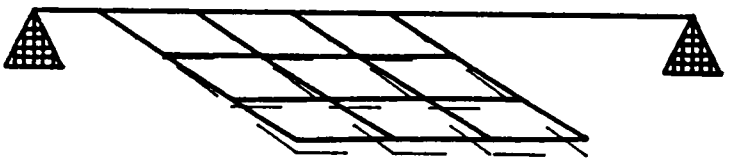

Experimental

Figure 6. Hanging Grid Mode Shapes-Mode 1: Analytical on right, Experimental on left, Difference on top

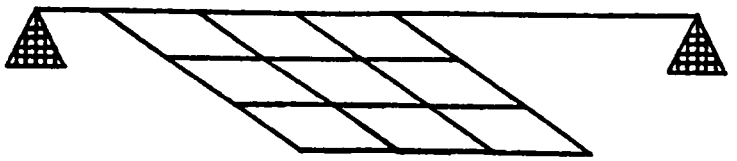

Difference

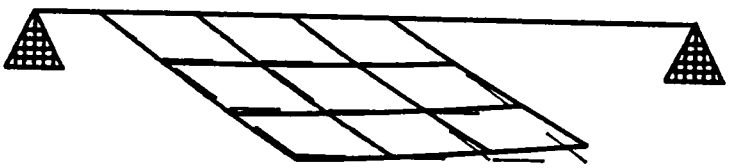

Analytical

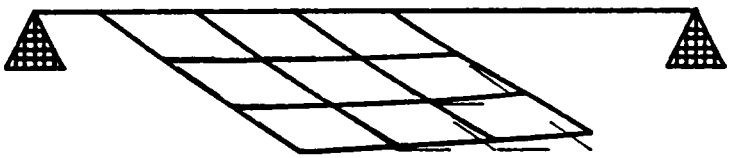

Experimental

Figure 7. Hanging Grid Mode Shapes-Mode 2: Analytical on right, Experimental on left, Difference on top

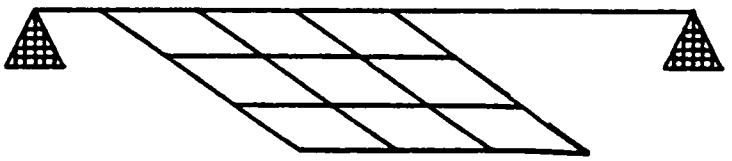

Difference

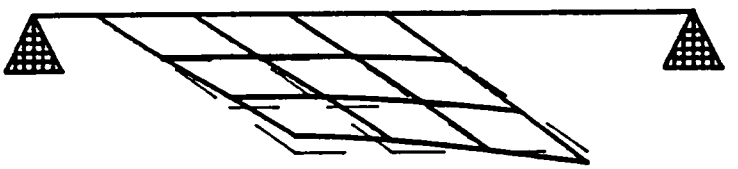

Analytical

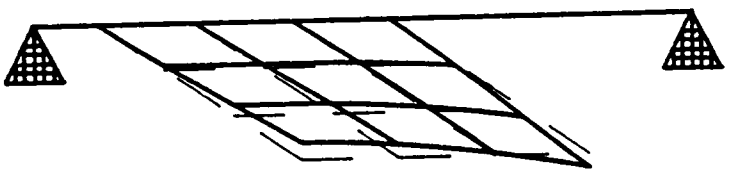

Experimental

Figure 8. Hanging Grid Mode Shapes-Mode 3: Analytical on right, Experimental on left, Difference on top

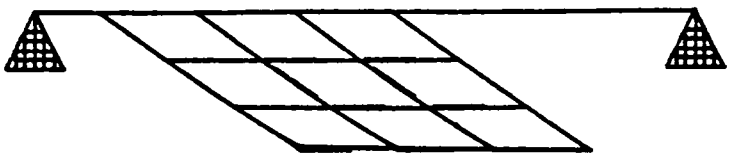

Difference

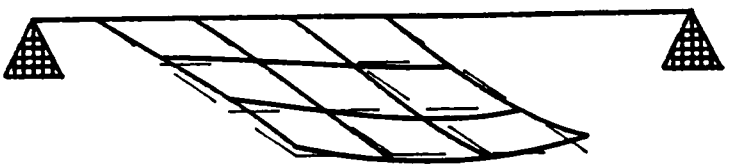

Analytical

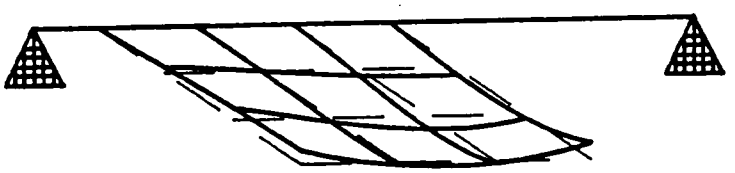

Experimental

Figure 9. Hanging Grid Mode Shapes-Mode 4: Analytical on right, Experimental on left, Difference on top

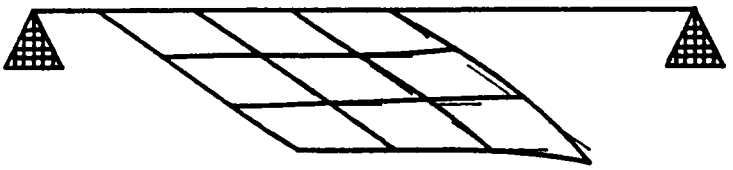

Difference

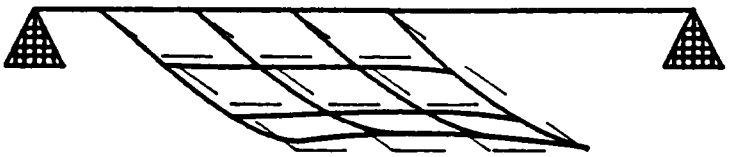

Analytical

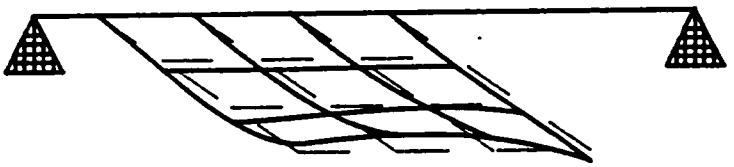

Experimental

Figure 10. Hanging Grid Mode Shapes-Mode 5: Analytical on right, Experimental on left, Difference on top

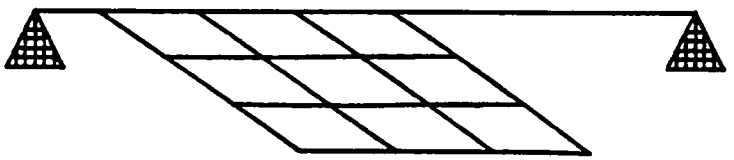

Difference

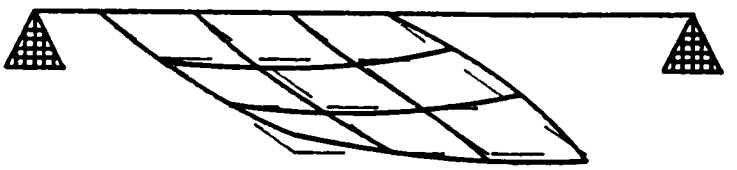

Analytical

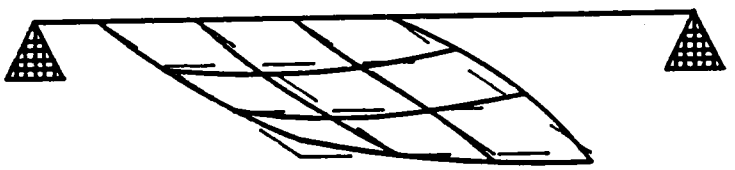

Experimental

Figure 11. Hanging Grid Mode Shapes-Mode 6: Analytical on right, Experimental on left, Difference on top

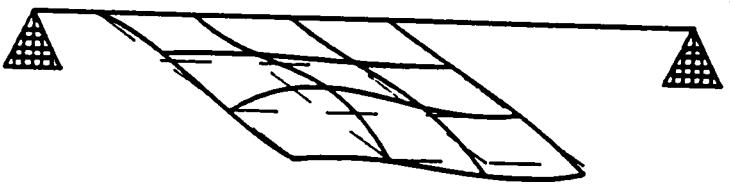

Difference

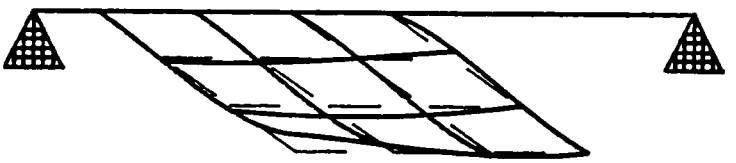

Analytical

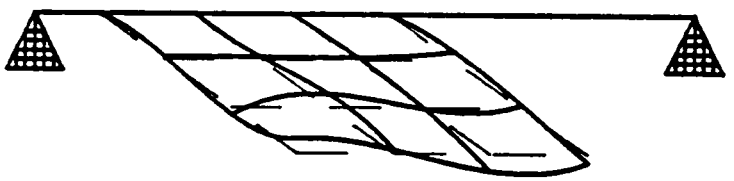

Experimental

Figure 12. Hanging Grid Mode Shapes-Mode 7: Analytical on right, Experimental on left, Difference on top

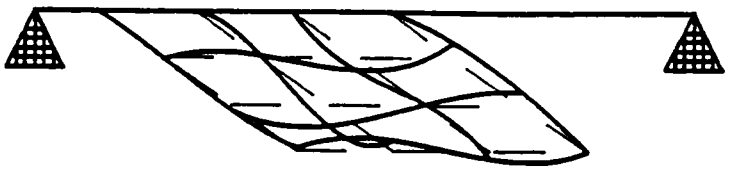

Difference

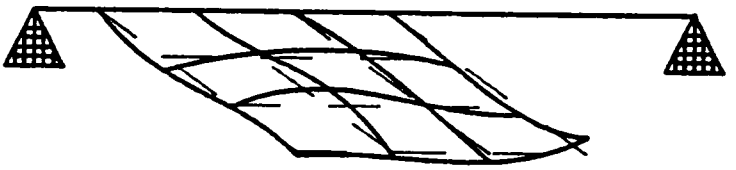

Analytical

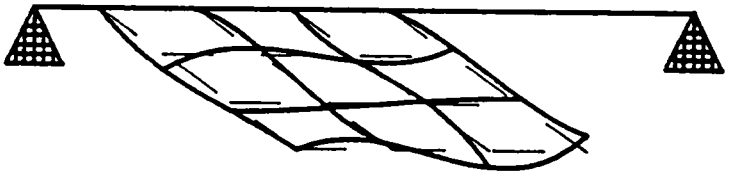

Experimental

Figure 13. Hanging Grid Mode Shapes-Mode 8: Analytical on right, Experimental on left, Difference on top

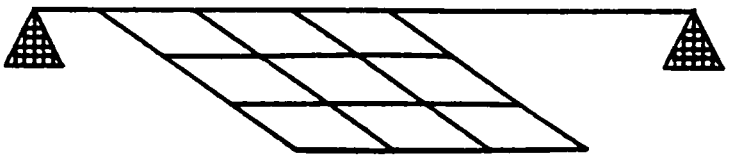

Difference

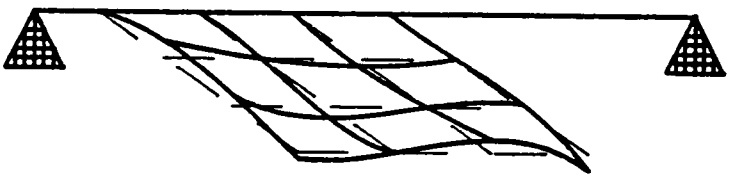

Analytical

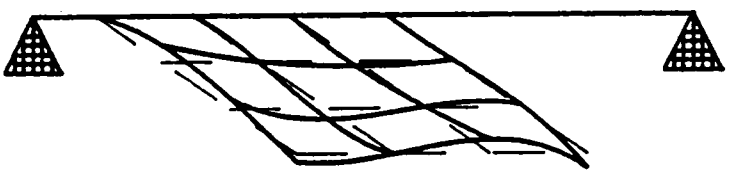

Experimental

Figure 14. Hanging Grid Mode Shapes-Mode 9: Analytical on right, Experimental on left, Difference on top

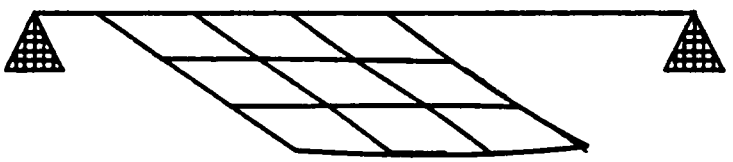

Difference

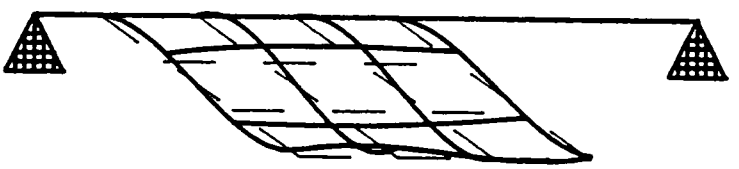

Analytical

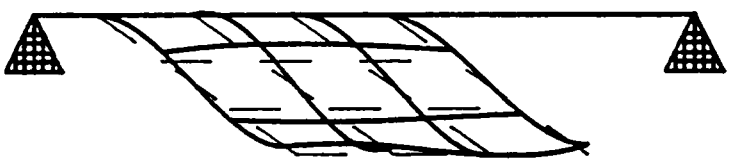

Experimental

Figure 15. Hanging Grid Mode Shapes-Mode 10: Analytical on right, Experimental on left, Difference on top

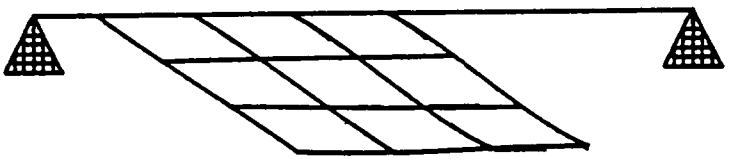

Difference

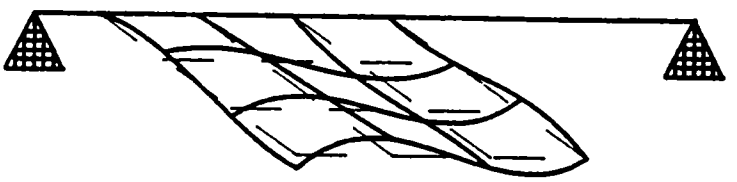

Analytical

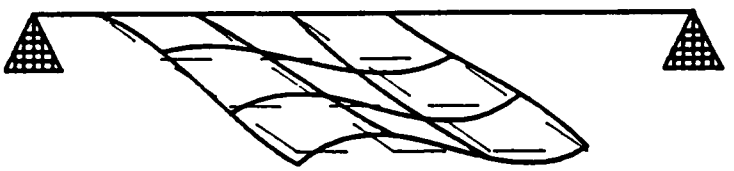

Experimental

Figure 16. Hanging Grid Mode Shapes-Mode 11: Analytical on right, Experimental on left, Difference on top

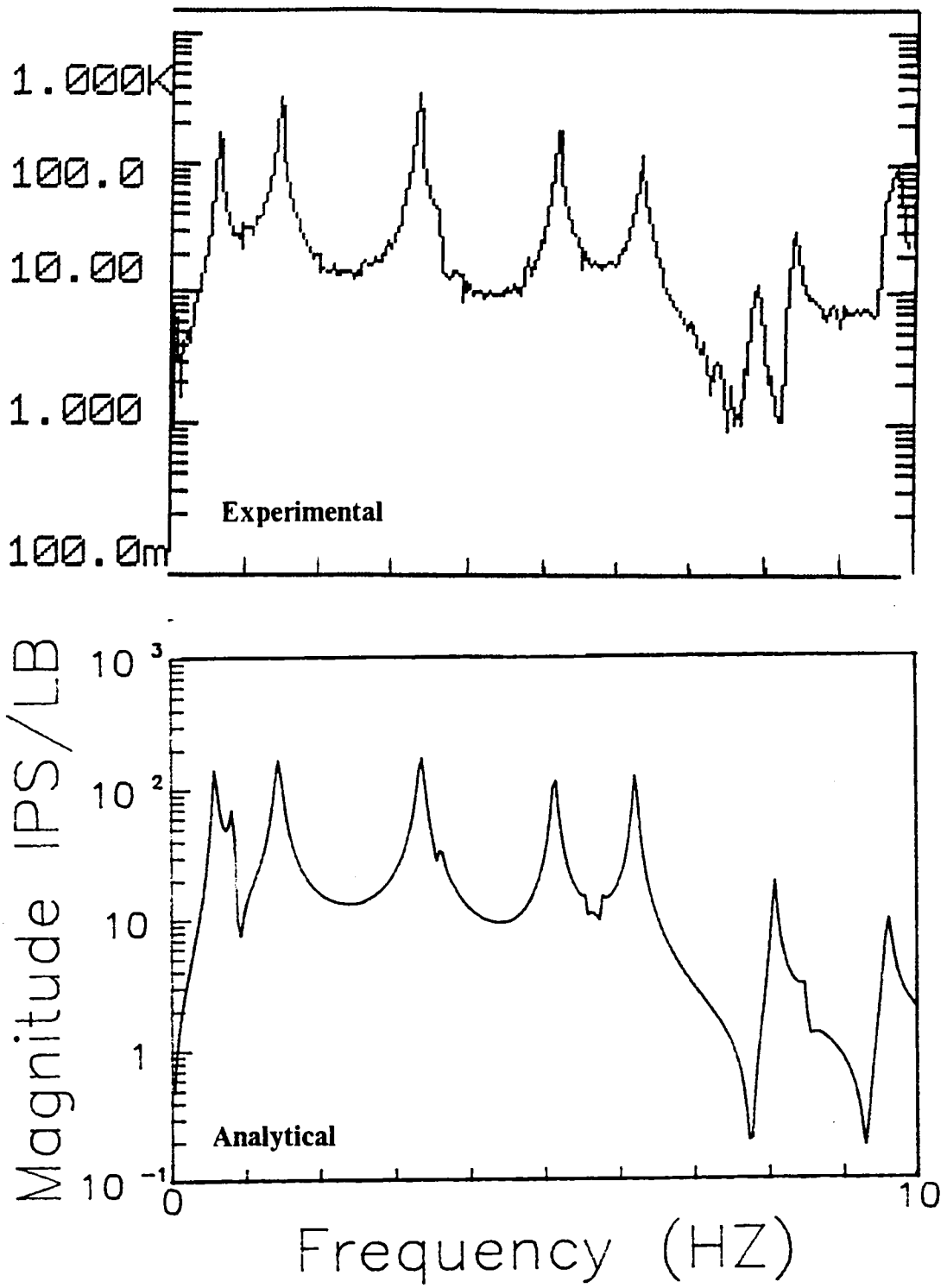

Figure 17. Hanging Grid Velocity Frequency Response Functions 1/4: For the hanging grid structure, Excitation at joint 4 response at joint 1

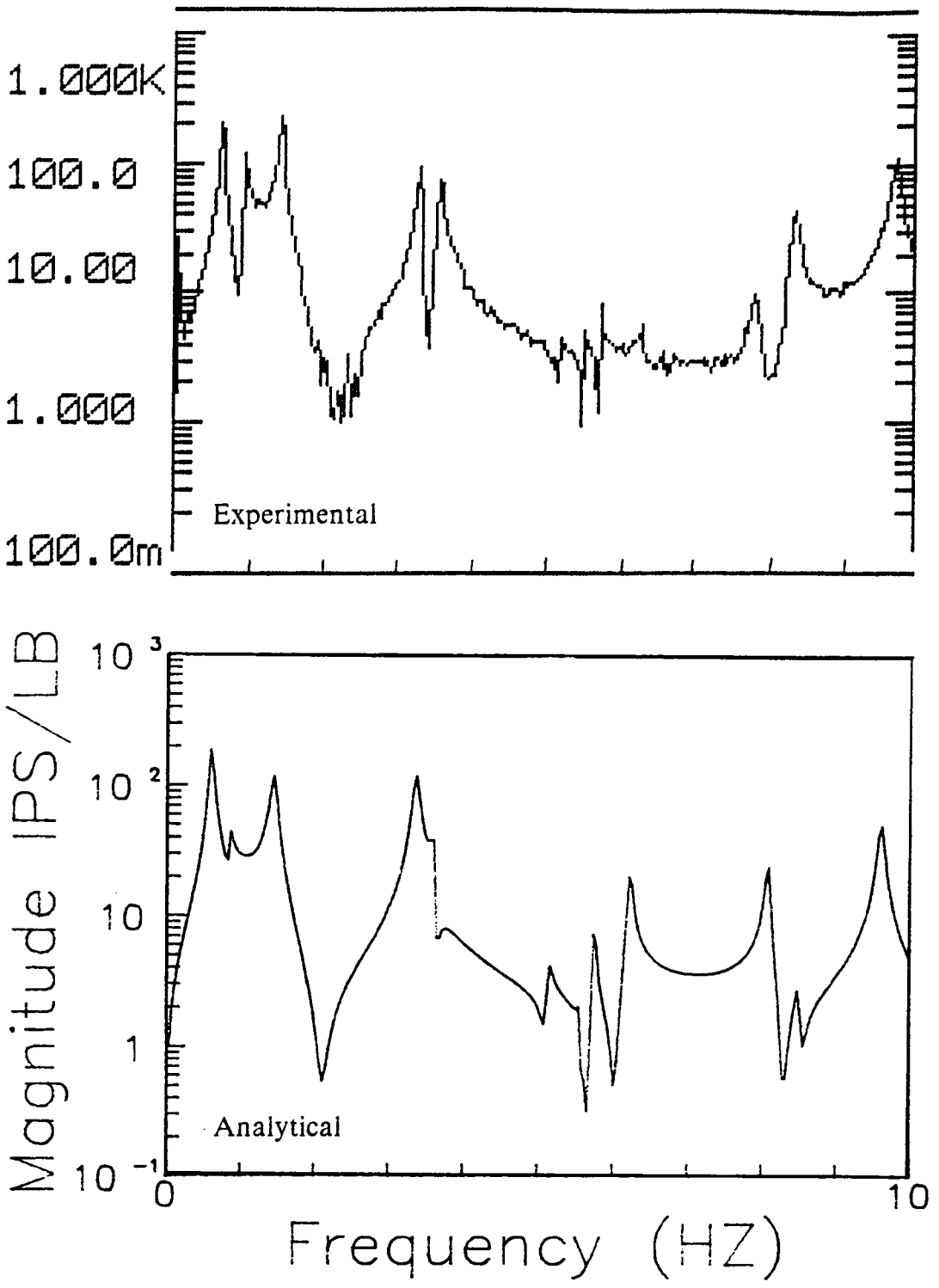

Figure 18. Hanging Grid Velocity Frequency Response Functions 2/4: For the hanging grid structure, Excitation at joint 4 response at joint 2

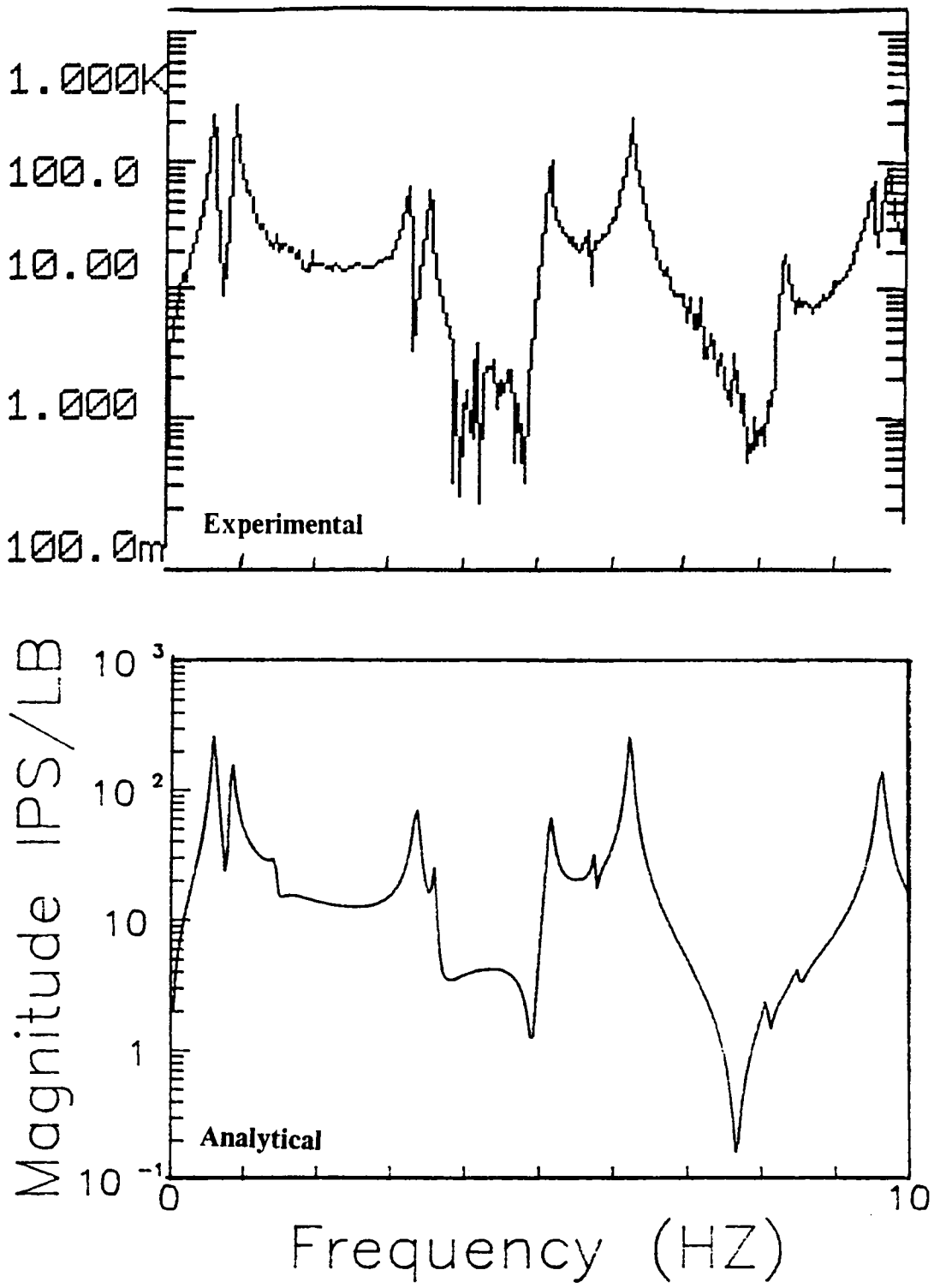

Figure 19. Hanging Grid Velocity Frequency Response Functions 3/4: For the hanging grid structure, Excitation at joint 4 response at joint 3

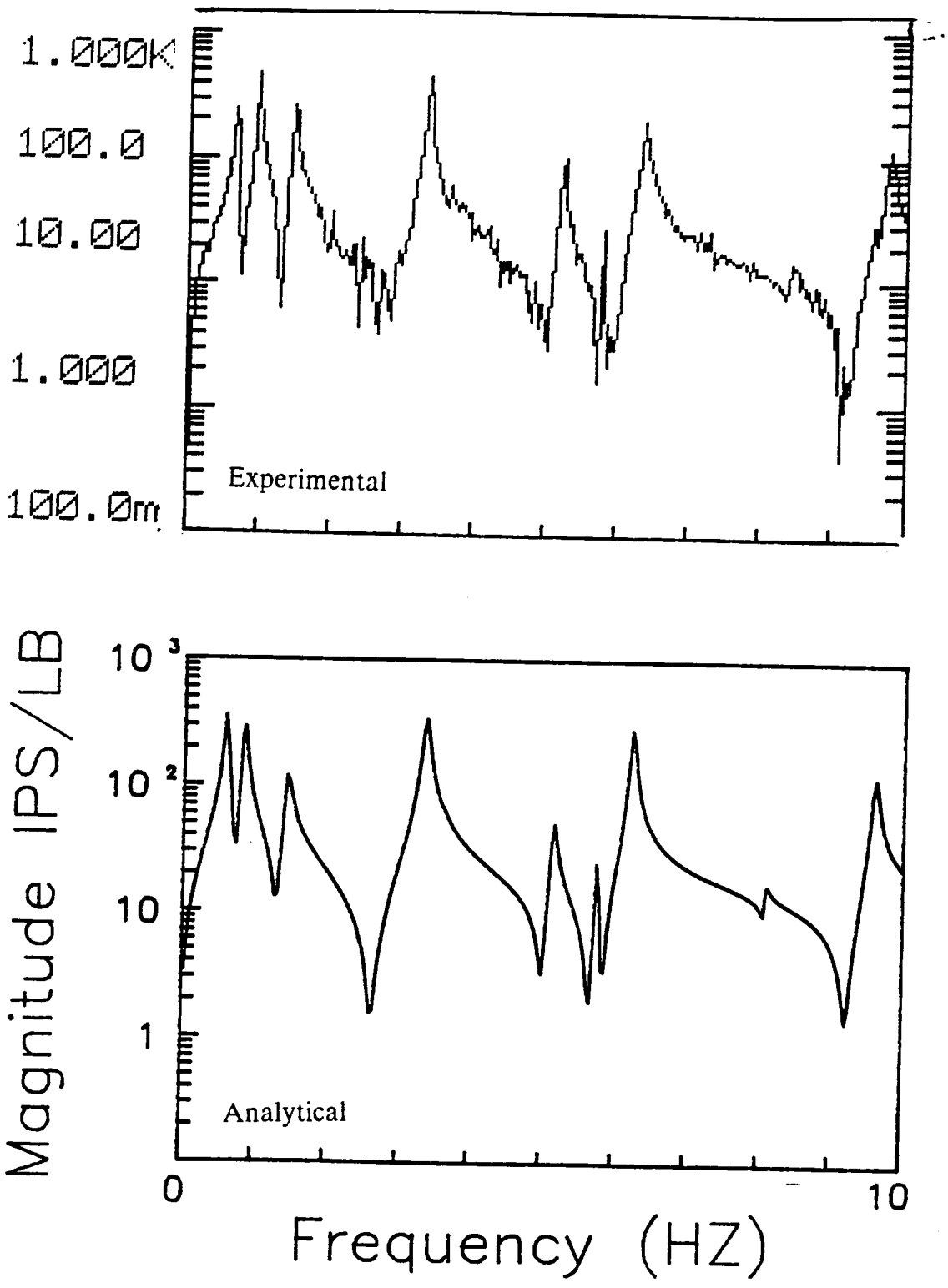

Figure 20. Hanging Grid Velocity Frequency Response Functions 4/4: For the hanging grid structure, Excitation at joint 4 response at joint 4

Chapter 3

Model Reduction and Correction

The equations of motion for a structure with n degrees of freedom (DOF) and controlled by n_c actuators are

$$\mathbf{m}\ddot{\mathbf{q}}(t) + \mathbf{c}\dot{\mathbf{q}}(t) + \mathbf{k}\mathbf{q}(t) = \mathbf{U}\mathbf{u}(t). \tag{3.1}$$

where **m**, **c**, and **k** are the nxn mass, inherent viscous damping, and stiffness matrices, respectively. It is assumed that **c** does not couple the undamped modes of vibration. **q** is an $nx1$ vector of physical or generalized displacement coordinates, and **U** is an nxn_c applied load distribution matrix relating the n_cx1 control input vector **u** to the structural DOFs. The system matrices are assumed to be constant.

Including uncertainties and random excitation in the form of a vector $\mathbf{w}_1(t)$, the equations of motion are written for the state vector $\mathbf{x} = [\mathbf{q}^T, \dot{\mathbf{q}}^T]^T$ as

$$\dot{\mathbf{x}}(t) = \mathbf{A}\mathbf{x}(t) + \mathbf{B}\mathbf{u}(t) + \mathbf{w}_1(t) \tag{3.2}$$

$$\mathbf{A} = \begin{bmatrix} -\mathbf{m}^{-1}\mathbf{c} & -\mathbf{m}^{-1}\mathbf{k} \\ \mathbf{I} & \mathbf{0} \end{bmatrix}, \qquad \mathbf{B} = \begin{bmatrix} \mathbf{m}^{-1}\mathbf{U} \\ \mathbf{0} \end{bmatrix} \tag{3.3}$$

To prevent numerical ill-conditioning, it is desirable that the $\mathbf{q}$ and $\dot{\mathbf{q}}$ components of $\mathbf{x}$ have the same order of magnitude. This can be achieved by using the reciprocal of a typical frequency as the time unit. In the present work the time unit employed was 10^{-2} second (cs).

For reasonably complex structures, the finite element model is usually of high order and when put in state space form the order of the system is doubled. This makes Linear Quadratic (LQ) control laws computationally difficult to design and impossible to implement. Direct Rate Feedback (DRF) control laws would be possible to implement but extremely time consuming to design if any optimization was to be performed. Therefore, it is necessary to reduce the order of the system so that only the important dynamics and degrees-of-freedom (DOFs) are included.

In this study two methods of model reduction are investigated. Both methods retain physical DOFs (rather than modal amplitudes) as generalized coordinates. The first reduction method is based on the first n_R undamped modes of the system (Ref. 8) and preserves the original full model frequencies and mode shapes exactly for the retained DOFs. This method will be called the exact reduction method. The reduced vector of DOFs $\mathbf{q}_R$ is a subset of the DOFs in $\mathbf{q}$. The sec-

ond model reduction used was the Guyan static condensation method which retains the static behavior of the retained DOFs.

The original finite element model may not be accurate enough in frequencies or mode shapes and these inaccuracies will be transmitted to the reduced models. Also, the Guyan reduction method changes the frequencies and mode shapes of the higher frequency modes of the reduced model. Therefore, a correction to the reduced model is desired based on experimental results. The correction method used herein was first proposed by Baruch and Bar-Itzhak in 1978 (Ref. 11) and then extended to the process used herein by Baruch in 1982 (Ref. 12).

3.1 Model Reduction Methods

3.1.1 Exact Reduction

The equations of motion for the undamped full-order system in matrix form are

$$\mathbf{M}\ddot{\mathbf{q}}(t) + \mathbf{K}\mathbf{q}(t) = \mathbf{0} \tag{3.4}$$

from which the full order modal matrix $\mathbf{\Phi}$, natural frequency matrix $diag(\omega_i^2)$, and the modal mass matrix $diag(\mathrm{M}_i)$ are determined. Next, the DOFs and number of modes to be retained are selected based on the points of interest on the structure. The full order modal matrix is then reordered and partitioned so that

elements corresponding to the retained DOFs are in the upper lefthand part of the matrix.

$$\mathbf{\Phi} = \begin{bmatrix} \mathbf{\Phi}_R(n_R x n_R) & \mathbf{\Phi}_{12}(n_R x [n - n_R]) \\ \mathbf{\Phi}_{21}([n - n_R] x n_R) & \mathbf{\Phi}_{22}([n - n_R] x [n - n_R]) \end{bmatrix} \tag{3.5}$$

For the model reduction process, the reduced modal matrix $\mathbf{\Phi}_R$ is the only part of the full modal matrix used. The diagonal frequency and modal mass matrices are also reduced to n_R diagonal elements. Experimentally determined damping ratios ζ_i are used to calculate the reduced damping matrix. The reduced matrices needed for obtaining reduced system and control matrices $\mathbf{A}_R$ and $\mathbf{B}_R$ are then given as

$$\mathbf{m}_R^{-1}\mathbf{c}_R = \mathbf{\Phi}_R\,[diag(2\zeta_i\omega_i)]_R\,\mathbf{\Phi}_R^{-1} \tag{3.6}$$

$$\mathbf{m}_R^{-1}\mathbf{k}_R = \mathbf{\Phi}_R\,[diag(\omega_i^2)]_R\,\mathbf{\Phi}_R^{-1} \tag{3.7}$$

$$\mathbf{m}_R^{-1}\mathbf{U}_R = \mathbf{\Phi}_R\,[diag(\mathrm{M}_i^{-1})]_R\,\mathbf{\Phi}_R^T\mathbf{U}_R \tag{3.8}$$

This reduction method preserves the analytic modes and frequencies of the finite element model exactly.

3.1.2 Guyan Reduction

The second model reduction scheme used herein is the Guyan Reduction (Ref. 1) which redistributes the system properties to a subset of the total number

of DOFs preserving the static behavior of the finite element model. This reduction process operates on the mass and stiffness matrices directly not through the modal properties. To reduce the stiffness matrix to the desired DOFs, we first partition it in the same manner the full modal matrix was partitioned in the exact reduction.

$$\mathbf{K}_{Part} = \begin{bmatrix} \mathbf{K}_{11}(n_R x n_R) & \mathbf{K}_{12}(n_R x [n - n_R]) \\ \mathbf{K}_{21}([n - n_R] x n_R) & \mathbf{K}_{22}([n - n_R] x [n - n_R]) \end{bmatrix} \tag{3.9}$$

The static equilibrium equation is now

$$\mathbf{K}_{Part}\, \mathbf{q}_{Part} = \mathbf{F}_{Part} \tag{3.10}$$

$$\mathbf{K}_{Part} = \begin{bmatrix} \mathbf{K}_{11} & \mathbf{K}_{12} \\ \mathbf{K}_{21} & \mathbf{K}_{22} \end{bmatrix}, \quad \mathbf{q}_{Part} = \begin{bmatrix} \mathbf{q}_1 \\ \mathbf{q}_2 \end{bmatrix}, \quad \mathbf{F}_{Part} = \begin{bmatrix} \mathbf{F}_1 \\ \mathbf{F}_2 \end{bmatrix}. \tag{3.11}$$

Solving the second row of equation 3.10 we get

$$\mathbf{q}_2 = \mathbf{K}_{22}^{-1}\, \mathbf{F}_2 - \mathbf{K}_{11}^{-1}\, \mathbf{K}_{12}^{T}\, \mathbf{q}_1 \tag{3.12}$$

$\mathbf{q}_2$ is then substituted back into the top row of equation 3.10 to get

$$[\mathbf{K}_{11} - \mathbf{K}_{21}\, \mathbf{K}_{22}^{-1}\, \mathbf{K}_{12}^{T}]\, \mathbf{q}_1 = \mathbf{F}_1 - \mathbf{K}_{12}\, \mathbf{K}_{22}^{-1}\, \mathbf{F}_2 \tag{3.13}$$

The reduced stiffness matrix is then defined as

$$\mathbf{K}_R = \mathbf{K}_{11} - \mathbf{K}_{21}\, \mathbf{K}_{22}^{-1}\, \mathbf{K}_{12}^{T} \tag{3.14}$$

To obtain the reduced mass matrix, consider the equation

$$\mathbf{q}_2 = \mathbf{G}_0 \mathbf{q}_1, \quad \mathbf{G}_0 = -\mathbf{K}_{22}^{-1} \mathbf{K}_{12}^T \tag{3.15}$$

as a set of rigid constraints. The reduced mass matrix is then found to be

$$\mathbf{M}_R = \mathbf{M}_{11} + \mathbf{M}_{12} \mathbf{G}_0 \mathbf{K}_{12} + \mathbf{G}_0^T \mathbf{M}_{12}^T + \mathbf{G}_0^T \mathbf{G}_0 \tag{3.16}$$

3.2 Reduced Model Correction

It is unusual to have good agreement between analytically predicted and experimentally measured vibration frequencies and modes of complex structures. Since the analytical modes and frequencies are used in the control system design it is important to correct the analytical model to agree with experimental data. Several methods for model corrections are available. The correction method used herein was first proposed by Baruch and Bar-Itzhak in 1978 (Ref. 11) and then extended to the process described next by Baruch in 1982 (Ref. 12). Experimentally measured frequencies and mode shapes are used as the reference basis for this correction. First the experimental mode shapes are normalized with respect to the uncorrected reduced mass matrix,

$$\hat{\mathbf{\Phi}}_i = \mathbf{\Phi}_{Ri} (\mathbf{\Phi}_{Ri}^T \mathbf{m}_R \mathbf{\Phi}_{Ri})^{-1/2} \tag{3.17}$$

and then the correction to the mass matrix is

$$\hat{\mathbf{m}}_R = \mathbf{m}_R - \mathbf{m}_R \hat{\mathbf{\Phi}} (\hat{\mathbf{\Phi}}^T \mathbf{m}_R \hat{\mathbf{\Phi}})^{-1} (\hat{\mathbf{\Phi}}^T \mathbf{m}_R \hat{\mathbf{\Phi}} - \mathbf{I}) (\hat{\mathbf{\Phi}}^T \mathbf{m}_R \hat{\mathbf{\Phi}})^{-1} \hat{\mathbf{\Phi}}^T \mathbf{m}_R \quad (3.18)$$

where $\hat{\mathbf{\Phi}}$ is the corrected reduced modal matrix. The correction to the stiffness matrix is given in terms of a diagonal matrix of experimental frequencies Ω^2 as

$$\hat{\mathbf{k}}_R = \mathbf{k}_R - \mathbf{k}_R \hat{\mathbf{\Phi}} \hat{\mathbf{\Phi}}^T \hat{\mathbf{m}}_R - \hat{\mathbf{m}}_R \hat{\mathbf{\Phi}} \hat{\mathbf{\Phi}}^T \mathbf{k}_R + \hat{\mathbf{m}}_R \hat{\mathbf{\Phi}} \hat{\mathbf{\Phi}}^T \mathbf{k}_R \hat{\mathbf{\Phi}} \hat{\mathbf{\Phi}}^T \hat{\mathbf{m}}_R + \hat{\mathbf{m}}_R \hat{\mathbf{\Phi}} \Omega^2 \hat{\mathbf{\Phi}}^T \mathbf{m}_R \quad (3.19)$$

The damping matrix is determined from the experimental frequencies, damping ratios and mode shapes as

$$\hat{\mathbf{m}}_R^{-1} \hat{\mathbf{c}}_R = \hat{\mathbf{\Phi}}_R [diag(2\zeta_i \omega_i)]_R \hat{\mathbf{\Phi}}_R^{-1} \quad (3.20)$$

3.3 Reduction and Correction Results on Grid Structure

The first reduced model used in this study was obtained with the exact reduction method because this method does not alter the analytic frequencies. For this reduction, we retained the 12 translations at the joints on the aluminum grid since they have the largest displacements. When the open loop VFRFs were compared, we noticed significant differences between the experiment and analysis (Figs. 17-20). Therefore, we attempted to correct the exact reduced model with experimental mode shapes and frequencies.

It is generally assumed in structural analysis that the mass matrix is better known than the stiffness matrix. Therefore, any correction made to the mass

matrix should be minimal. Equation (3.18) is the correction to the mass matrix and the term that controls the amount of change is $(\hat{\mathbf{\Phi}}^T\mathbf{m}_R\hat{\mathbf{\Phi}} - \mathbf{I})$. If the experimental mode shapes are perfectly orthogonal with respect to the original reduced mass matrix then there is no change to that matrix. On the other hand if $\hat{\mathbf{\Phi}}^T\mathbf{m}_R\hat{\mathbf{\Phi}}$ the orthogonality matrix has a large number of off diagonal terms of significant size, there will be large changes to the mass matrix.

For this reduced model, the orthogonality matrix (Table 4) had many large off-diagonal terms with a maximum of 0.8 and an average of absolute values of 0.23, indicating poor orthogonality with this mass matrix. Applying the correction procedure to this reduced model in a sequential fashion, (first mode 1, then modes 1 and 2, etc.), altered not only the modes being corrected but also severely altered higher frequency modes. This indicates that this model is not a good model for this correction procedure.

Next we used the Guyan reduction with various sets of DOFs retained to find a set of DOFs which produced a minimum degradation of accuracy in the higher frequencies. This was obtained with DOFs consisting of the displacements at joints 1-9 and 12 on the aluminum grid and the rotations of the ball bearing supports of the top beam. Table 5 presents the frequencies produced by this model. Notice that the frequencies obtained from the Guyan reduced model begin to diverge significantly from the full-model frequencies at mode 8.

The orthogonality of the Guyan reduced mass matrix with the experimental mode shapes is improved over the orthogonality of the exact reduction (Table 6). The maximum off-diagonal element in this case is 0.58 and the average of the

absolute values of the off-diagonal terms is 0.13. Applying the correction procedure to the Guyan reduced model in the same sequential manner as before, revealed a different behavior pattern than the exact reduction. The successive application of each additional mode either did not alter the higher frequencies or it improved them. In contrast applying this process to the exact reduced model produced large adverse changes in the higher modes. Eleven experimental modes were used in this process and their application improved the twelfth frequency in the Guyan model from 11.32 Hz to 9.84 Hz.

To determine if the very poor orthogonality of the exact reduced mass matrix was due to the DOFs retained in the model or the reduction method, we used the DOFs from the Guyan reduction in the exact reduction. The maximum element of this orthogonality matrix was 0.72 and the average of the absolute values of the off-diagonal elements was 0.29. This indicates that it is the reduction process that makes the difference not the DOFs.

Table 4. Orthogonality Matrix for 11 Experimental Modes with Exact Reduced Mass Matrix - Hanging Grid

Mode	1	2	3	4	5	6	7	8	9	10	11
1	1.00	0.71	0.12	0.37	-0.10	0.04	0.00	0.25	-0.19	0.29	0.08
2	0.71	1.00	-0.59	0.25	-0.18	-0.11	-0.32	0.60	-0.33	0.20	0.30
3	0.12	-0.59	1.00	-0.01	0.39	0.24	0.42	-0.57	0.24	-0.05	-0.30
4	0.37	0.25	-0.01	1.00	-0.19	-0.01	-0.13	0.17	-0.26	0.28	-0.06
5	-0.10	-0.18	0.39	-0.19	1.00	0.09	-0.06	-0.25	0.09	-0.05	-0.12
6	0.04	-0.11	0.24	-0.01	0.09	1.00	0.59	0.17	0.03	0.00	-0.13
7	0.00	-0.32	0.42	-0.13	-0.06	0.59	1.00	0.34	-0.35	0.21	0.18
8	0.25	0.60	-0.57	0.17	-0.25	0.17	0.34	1.00	-0.80	0.33	0.41
9	-0.19	-0.33	0.24	-0.26	0.09	0.03	-0.35	-0.80	1.00	-0.23	-0.05
10	0.29	0.20	-0.05	0.28	-0.05	0.00	0.21	0.33	-0.23	1.00	0.10
11	0.08	0.30	-0.30	-0.06	-0.12	-0.13	0.18	0.41	-0.05	0.10	1.00

Table 5. Reduced Model Frequencies (Hz) - Hanging Grid

Mode No.	Full Model and Exact Red.	Guyan Red.	Experiment
1	0.593	0.593	0.687
2	0.840	0.841	0.949
3	1.45	1.45	1.47
4	3.35	3.43	3.33
5	3.60	3.68	3.64
6	5.14	5.26	5.22
7	5.57	5.77	5.57
8	5.75	6.51	5.78
9	6.22	8.76	6.36
10	8.08	9.51	7.89
11	8.50	10.08	8.39
12	9.60	11.32	9.60

Table 6. Orthogonality Matrix for 11 Experimental Modes with Guyan Reduced Mass Matrix - Hanging Grid

Mode	1	2	3	4	5	6	7	8	9	10	11
1	1.00	-0.19	0.01	0.05	-0.03	0.06	0.09	0.03	0.17	0.34	0.14
2	-0.19	1.00	0.16	0.01	0.12	0.01	0.19	-0.01	0.00	0.05	0.13
3	0.01	0.16	1.00	0.08	0.26	0.06	-0.28	-0.02	0.10	0.30	-0.10
4	0.05	0.01	0.08	1.00	-0.11	-0.05	0.12	0.06	-0.20	-0.24	-0.09
5	-0.03	0.12	0.26	-0.11	1.00	0.04	0.10	-0.10	-0.11	-0.23	0.04
6	0.06	0.01	0.06	-0.05	0.04	1.00	-0.58	0.14	-0.11	-0.23	0.04
7	0.09	0.19	-0.28	0.12	0.10	-0.58	1.00	-0.44	0.31	-0.42	-0.14
8	0.03	-0.01	-0.02	0.06	-0.10	0.14	-0.44	1.00	-0.24	0.06	-0.06
9	0.16	0.00	0.10	-0.20	-0.12	-0.02	0.31	-0.24	1.00	-0.12	0.15
10	0.34	0.05	0.30	-0.24	-0.23	-0.20	-0.42	0.06	-0.12	1.00	0.11
11	0.14	0.13	-0.10	-0.09	0.04	-0.01	-0.14	0.06	0.15	0.11	1.00

Chapter 4

Control System Design

A standard state space approach was used to develop the control systems. The equation of motion including system uncertainties is

$$\dot{\mathbf{x}} = \mathbf{A}\mathbf{x} + \mathbf{B}\mathbf{u} + \mathbf{w}_1 \tag{4.1}$$

and the measurement equation with noise is

$$\mathbf{y} = \mathbf{C}\mathbf{x} + \mathbf{w}_2 \tag{4.2}$$

All of the control designs use some form of linear feedback

$$\mathbf{u} = -\mathbf{F}\mathbf{x} \tag{4.3}$$

where determining **F** is the object of the control system design process.

4.1 Linear Quadratic Control

4.1.1 Linear Quadratic Regulator

The standard steady-state, deterministic (i.e. $\mathbf{w}_1 = \mathbf{0}$) Linear Quadratic Regulator (LQR) has a performance index (Ref. 56) of the form

$$J = \int_0^\infty [\mathbf{x}(t)^T \mathbf{Q}\mathbf{x}(t) + \mathbf{u}(t)^T \mathbf{R}\mathbf{u}(t)]dt \tag{4.4}$$

where $\mathbf{Q}$ (Ref. 56) is the positive semi-definite state weighting matrix ($2nx2n$) and R is the positive definite control weighting matrix ($n_c x n_c$). These matrices are selected here so as to insure a minimum value ζ_L for the damping ratios of the first n_m modes. The optimal linear regulator has the form

$$\mathbf{u}(t) = -\mathbf{F}\,\mathbf{x}(t), \qquad \mathbf{F} = \mathbf{R}^{-1}\mathbf{B}^T\mathbf{S} \tag{4.5}$$

where $\mathbf{S}$ is found by solving an algebraic matrix Riccati equation

$$\mathbf{A}^T\mathbf{S} + \mathbf{S}\mathbf{A} - \mathbf{S}\mathbf{B}\mathbf{R}^{-1}\mathbf{B}^T\mathbf{S} + \mathbf{Q} = \mathbf{0}. \tag{4.6}$$

LQR control assumes that there are no uncertainties in the system (i.e. $\mathbf{w}_1 = 0$ Eq. (4.1)), that there is no measurement noise ($\mathbf{w}_2 = 0$ Eq. (4.2)), and that all state variables ($\mathbf{q}$ and $\dot{\mathbf{q}}$) can be measured. The optimum value of the performance index with a given vector $\mathbf{x}_0$ of initial conditions is

$$J_{\min} = \mathbf{x}_0^T \mathbf{S}\, \mathbf{x}_0 \tag{4.7}$$

The initial conditions chosen for comparison are the first n_f open-loop mode shapes (ϕ), each normalized with a maximum deflection of one inch, $\mathbf{x}_0^T = [0, \phi_i^T]$.

4.1.2 Linear Quadratic Gaussian Control

Since we cannot measure all of the states and measurement noise is present, we obtain an estimate $\mathbf{x}_{est}$ to the state with an observer that solves

$$\dot{\mathbf{x}}_{est}(t) = \mathbf{A}\mathbf{x}_{est}(t) + \mathbf{B}\mathbf{u}(t) + \mathbf{K}[\mathbf{y}(t) - \mathbf{C}\mathbf{x}_{est}(t)] \tag{4.8}$$

where $\mathbf{y}(t)$ is determined by Eq. (4.2). The observer is calculated on the basis of a zero initial state for the estimated variable. $\mathbf{y}(t)$ is the n_sx1 vector of noisy measurements and $\mathbf{C}$ is the n_sxn observation matrix. n_s is the number of sensors used. Both state excitation noise ($\mathbf{w}_1$) and state observation noise ($\mathbf{w}_2$) are assumed to be uncorrelated Gaussian white noise processes with zero mean and intensity (covariance) matrices $\mathbf{V}_1$ and $\mathbf{V}_2$. $\mathbf{K}$ is the observer gain matrix to be determined (Ref. 56). In this study a Kalman filter is used as the observer. So the filter gain matrix is found through the solution of another Riccati equation.

$$(\mathbf{A} + \alpha\mathbf{I})\,\mathbf{S}_f + \mathbf{S}_f(\mathbf{A} + \alpha\mathbf{I})^T - \mathbf{S}_f\mathbf{C}^T\mathbf{V}_2^{-1}\mathbf{C}\mathbf{S}_f + \mathbf{V}_1 = 0 \tag{4.9}$$

This Riccati equation depends on the assumed system ($\mathbf{V}_1$) and measurement covariance noise matrices ($\mathbf{V}_2$) and the prescribed stability margin, ("alpha shift") ,(Refs. 57 and 58) of the filter poles. The alpha shift requires that the real parts of each filter eigenvalue be more negative than $-\alpha$. The filter gain matrix is then given as

$$\mathbf{K} = \mathbf{S}_f \mathbf{C}^T \mathbf{V}_2^{-1} \tag{4.10}$$

With this optimal estimate of the state vector, the control equation is

$$\mathbf{u}(t) = -\mathbf{F}\mathbf{x}_{est}(t). \tag{4.11}$$

The alpha shift was found to have the greatest effect on the eigenvalues of the filter and the noise matrices had the greatest effect on the performance of the system. Therefore, the noise matrices were selected to reduce the effect of the observer on the performance of combined observer/regulator system. This combined system is called Linear Quadratic Gaussian (LQG) control.

Mathematically, LQG control is developed from the original system Eq. (4.1) and Eq. (4.5). Substituting in for the measured state vector **y** and the control force **u** in the two equations, we get

$$\dot{\mathbf{x}}_{est} = (\mathbf{A} - \mathbf{BF})\mathbf{x}_{est} + \mathbf{KC}(\mathbf{x} - \mathbf{x}_{est}) \tag{4.12}$$

and

$$\dot{\mathbf{x}} = \mathbf{A}\,\mathbf{x} - \mathbf{BF}\,\mathbf{x}_{est} \tag{4.13}$$

Subtracting equation 4.12 from 4.13 we get an equation for the error in the state estimate

$$\dot{\mathbf{x}} - \dot{\mathbf{x}}_{est} = (\mathbf{A} - \mathbf{KC})(\mathbf{x} - \mathbf{x}_{est}) \tag{4.14}$$

Subtracting and adding **BFx** to equation 4.13 we get

$$\dot{\mathbf{x}} = (\mathbf{A} - \mathbf{BF})\mathbf{x} + \mathbf{BF}(\mathbf{x} - \mathbf{x}_{est}) \tag{4.15}$$

Letting **e** represent $\mathbf{x} - \mathbf{x}_{est}$ and arranging the state vector **x** and the error vector **e** in an augmented vector $\bar{\mathbf{x}}$ we get

$$\dot{\bar{\mathbf{x}}}(t) = \bar{\mathbf{A}}\,\bar{\mathbf{x}}(t), \qquad \bar{\mathbf{A}} = \begin{bmatrix} \mathbf{A} - \mathbf{BF} & \mathbf{BF} \\ \mathbf{0} & \mathbf{A} - \mathbf{KC} \end{bmatrix} \tag{4.16}$$

and

$$\bar{\mathbf{x}}(t) = \begin{Bmatrix} \mathbf{x}(t) \\ \mathbf{e}(t) \end{Bmatrix} \tag{4.17}$$

The optimal value of the performance index equation (4.4) is given as

$$J = \int_0^\infty [\bar{\mathbf{x}}^T(t)\bar{\mathbf{Q}}\bar{\mathbf{x}}(t)]dt \tag{4.18}$$

where

$$\bar{\mathbf{Q}} = \begin{bmatrix} \mathbf{Q} + \mathbf{F}^T\mathbf{RF} & -\mathbf{F}^T\mathbf{RF} \\ -\mathbf{F}^T\mathbf{RF} & \mathbf{F}^T\mathbf{RF} \end{bmatrix} \tag{4.19}$$

or

$$J_{\min} = \bar{\mathbf{x}}_0^T \bar{\mathbf{P}} \bar{\mathbf{x}}_0 \tag{4.20}$$

where the $4nx4n$ matrix $\mathbf{P}$ is the solution of the Lyapunov equation

$$\bar{\mathbf{A}}^T \bar{\mathbf{P}} + \bar{\mathbf{P}}\bar{\mathbf{A}} + \bar{\mathbf{Q}} = 0 \tag{4.21}$$

The initial observer state estimate is assumed to be $\mathbf{x}_{0,est} = 0$ so the initial augmented initial state is

$$\bar{\mathbf{x}}_0 = \begin{Bmatrix} \mathbf{x}_0 \\ \mathbf{x}_0 \end{Bmatrix} \tag{4.22}$$

4.1.3 LQG Control with Reduced Model

To investigate the effect of model reduction, we analyze a full-order model of the structure connected to a controller designed for the reduced model. The combined structure/controller is a linear system of order $2n + 2n_R$,

$$\dot{\mathbf{x}}_E(t) = \mathbf{A}_E \mathbf{x}_E(t) \tag{4.23}$$

where

$$\mathbf{A}_E = \begin{bmatrix} \mathbf{A} & -\mathbf{B}\mathbf{F}_R \\ \mathbf{K}_R\mathbf{C} & \mathbf{A}_R - \mathbf{K}_R\mathbf{C}_R - \mathbf{B}_R\mathbf{F}_R \end{bmatrix} \tag{4.24}$$

and

$$\mathbf{x}_E = \begin{Bmatrix} \mathbf{x}(t) \\ \mathbf{x}_{R,est} \end{Bmatrix} \tag{4.25}$$

A subscript R denotes the reduced form of the corresponding matrix.

The quadratic performance index for the reduced order control system can be evaluated as

$$J_{\min} = \mathbf{x}_{E0}^T \mathbf{P}_E \mathbf{x}_{E0} \tag{4.26}$$

where the matrix $\mathbf{P}_E$ of order $2n + 2n_R$ is the solution, (Refs. 56 and 59), of the Lyapunov equation

$$\mathbf{A}_E^T \mathbf{P}_E + \mathbf{P}_E \mathbf{A}_E + \mathbf{Q}_E = \mathbf{0}, \tag{4.27}$$

with

$$\mathbf{Q}_E = \begin{bmatrix} \mathbf{Q} & \mathbf{0} \\ \mathbf{0} & \mathbf{F}_R^T \mathbf{R} \mathbf{F}_R \end{bmatrix} \tag{4.28}$$

We assume that the initial observer state estimate is $\mathbf{x}_{R0,est} = \mathbf{0}$, and therefore the augmented initial state is

$$\mathbf{x}_{E0}^T = \begin{Bmatrix} \mathbf{x}_0 \\ 0 \end{Bmatrix} \tag{4.29}$$

4.2 *Direct Rate Feedback Control*

4.2.1 Minimized Maximum Force Direct Rate Feedback Control

Minimized maximum force direct rate feedback control (MFDRF) is a special case of direct output feedback control. Active vibration damping is effected by pairs of colocated velocity sensors and force actuators. The number of control pairs (n_c) is typically much smaller than the order of **x**, and only a vector **y** of n_c velocity elements $\dot{q}_j$ of the state vector is fed back in the closed loop,

$$\mathbf{u}(t) = -\mathbf{D}\mathbf{y}(t) \tag{4.30}$$

Asymptotic system stability is guaranteed if the active damping matrix **D** ($n_c x n_c$) is positive definite because this form of active damping can only dissipate energy (Refs. 30, 36 and 60) We therefore require $\mathbf{D} > 0$ as a constraint and, additionally, impose minimum stability margins on selected modes of the structure.

The performance index selected here for obtaining the gain matrix **D** is the minimization of the maximum actuator force, assuming that each sensor has the same velocity bound. This index is chosen because the required stability margins limit the system response, so the objective function should minimize the size of the actuators. Assuming that each velocity bound is $\dot{q}_{\max}$, then the maximum possible actuator force $u_{\max}$ for each actuator is proportional to f_i

$$f_i = \frac{u_{\max}}{\dot{q}_{\max}} = \sum_{j=1}^{n_c} |d_{ij}| \qquad i = 1,...,n_c \tag{4.31}$$

The elements of **D** are then determined such that the control force ratio for each actuator is less than or equal to a value γ . The variable γ is then minimized subject to constraints. The optimum design problem is formulated as

$$\text{find} \quad \mathbf{D} \text{ to minimize } \gamma \tag{4.32}$$

$$\text{subject to } g_j = \zeta_j - \zeta_L \geq 0 \qquad j = 1,...,n_m$$

$$\mathbf{D} > 0 \text{ and } f_i \leq \gamma$$

where g_j are constraints on the stability of the closed loop system, expressed as lower limits (ζ_L) on the damping ratios (ζ_j) of the first n_m modes. The absolute value function does not have continuous derivatives at zero and is replaced by a quartic polynomial near zero (Ref. 59).

For comparison with the LQG design, the performance index of Eq. (4.4) is calculated for the MFDRF design, for a given set of initial conditions $\mathbf{x}_0$ as:

$$J_{\min} = \mathbf{x}_o^T \tilde{\mathbf{P}} \mathbf{x}_o \tag{4.33}$$

where $\tilde{\mathbf{P}}$ is obtained from the Lyapunov equation

$$\tilde{\mathbf{A}}^T \tilde{\mathbf{P}} + \tilde{\mathbf{P}} \tilde{\mathbf{A}} + \tilde{\mathbf{Q}} = \mathbf{0} \tag{4.34}$$

where

$$\tilde{\mathbf{A}} = \mathbf{A} - \mathbf{B}\,\mathbf{F}_D \tag{4.35}$$

and

$$\tilde{\mathbf{Q}} = \mathbf{Q} + \mathbf{F}_D^T \mathbf{R}\,\mathbf{F}_D \tag{4.36}$$

$\mathbf{F}_D$ is the gain matrix containing the elements of $\mathbf{D}$ as its only nonzero elements at the DOFs where control pairs are located.

4.2.2 Linear Quadratic Direct Rate Feedback Control

A second direct rate feedback control law is the Linear Quadratic Direct Rate Feedback (LQDRF) law based on the quadratic performance index of the LQ design. The LQ design minimizes the quadratic performance index for all initial conditions. This is impossible to achieve with direct rate feedback. Instead, the LQDRF law minimizes the quadratic performance index for initial conditions in the shape of a number n_f of natural vibration modes. That is

$$J_{LQDRF} = \max_{i=1,\ldots,n_f} J_i \quad \text{where} \quad J_i = \int_0^\infty [\mathbf{x}(t)^T \mathbf{Q}\mathbf{x}(t) + \mathbf{u}(t)^T \mathbf{R}\mathbf{u}(t)]dt \tag{4.37}$$

for $\mathbf{x}_0 = [0^T \ \phi_i^T]^T$. As with the other two control laws, lower limits (ζ_L) on the damping ratios, ζ_i of the first n_m modes are also imposed. Because the maximum

function in Eq. (4.37) can have discontinuous derivatives, an equivalent formulation is used for the LQDRF design as follows:

find β and the elements of **D** to minimize β

$$\text{such that} \quad J_i \leq \beta \quad i = 1,...,n_f \tag{4.38}$$

$$\text{subject to} \quad g_j = \zeta_j - \zeta_L \geq 0 \quad j = 1,..., n_m$$

$$\text{and} \quad \mathbf{D} > 0$$

The **Q** and **R** matrices here are the same as in the LQ design. The quadratic performance index is calculated as in Eqs. (4.33)-(4.36).

The optimization problems, Eqs. (4.31) and (4.37), were solved by using a general purpose software package - NEWSUMT-A (Ref. 61).

Chapter 5

Experimental Apparatus and Procedure

There are three basic types of equipment required to implement active control: sensors with their supporting equipment, actuators with their supporting equipment, and the controller which takes the sensed parameters and calculates the controlling force. To conduct experimental research, we also need equipment that excites the test structure and then measures and records the ensuing motion. Actual space structures will employ basically two types of sensors, structure-borne (such as accelerometers or piezoelectric devices), or remote (optical sensors). Actuators are certain to be structure-borne (reaction control thrusters, linear and rotational proof-mass actuators, or control moment gyroscopes), since, in space, there are no fixed supports to push against.

5.1 Sensors

In this study two types of simple, mechanically grounded, non-contacting sensors were used. The first, a displacement probe produced by Bently-Nevada, was used only to collect vibration data used in developing the mode shapes for the two structures. The probe was mounted on the support structure surrounding the test structures and maneuvered to within about 1/8-inch of a small steel target attached to the test structure. Signals produced by the Bently probes have a very high amplitude (1 volt per inch sensitivity) and are nearly noise free.

The second type of sensor, used in many previous studies (Refs. 28-30, 34-37, 49, 50, 54, 62 and 63). consists of a structure-borne conducting coil placed in an annular magnetic field generated by an externally supported magnetic field structure. The field structures were all mounted on adjustable bases so that the coil could be centered within the field structure. Movement of the conducting coil within the magnetic field produces a fluctuating voltage proportional to the velocity of the coil. These sensors produced linear signals over a small range (about 1/4-inch) with very little DC offset. One problem with these velocity sensors is that the unshielded wires leading from the coils act as antennas for radio frequency noise and the 60 cycle noise from the fluorescent overhead lights. The coil leads must be connected to a high input impedance to prevent back EMF that will distort the velocity signal and add a dissipative force to the structure. Small operational amplifiers wired in a unit gain circuit provided a one million million ohm impedance for this purpose.

5.2 *Force Actuators*

The type of actuator used in this study is based on the same principle as a loudspeaker. It consists of the same small conducting coil attached to the structure and the same type of magnetic field structure providing the annular magnetic field. To produce a force from this assembly, a current is applied through the coil producing a force as it reacts with the surrounding magnetic field. A voltage is input to the power amplifier which produces a controlled current. The current is controlled so that the fluctuating voltage produced by the motion of the coil does not affect the force applied to the structure.

5.3 *Controller*

A PC-1000 digital controller built by Systolic Systems Inc. processed the signals according to the control law being tested. The PC-1000 is a small desktop unit operated through a host IBM-PC personal computer. It has 16 channels available for input from sensors, a high speed array processor for doing calculations with the digitized sensor signals, and 16 channels for output signals to drive control actuators. The PC-1000 has a sampling rate variable from 2 to 2000 samples per second. When operated at high sampling rates with structural frequencies under about 20 Hz, the PC-1000 appears, for most practical purposes,

to be a continuous time (analog) instrument rather than a discrete time (digital) instrument since the phase lag produced by digital data acquisition and processing is very small. The actual time delay through the PC-1000 was found to be $1.35\Delta t$, where Δt is the sampling period.

The PC-1000's array processor performs one specific operation -- multiplication of a constant 48 x 48 coefficient matrix by a time-varying 48 x 1 vector -- at the specified sampling rate. Stated mathematically, the operation is

$$\begin{bmatrix} \mathbf{u}_k(16x1) \\ \mathbf{x}_{est,k+1}(32x1) \end{bmatrix} = \begin{bmatrix} \mathbf{F11}_{(16x16)} & \mathbf{F12}_{(16x32)} \\ \mathbf{F21}_{(32x16)} & \mathbf{F22}_{(32x32)} \end{bmatrix} \begin{bmatrix} \mathbf{y}_k(16x1) \\ \mathbf{x}_{est,k}(32x1) \end{bmatrix} \tag{5.1}$$

$\mathbf{y}_k$ is the vector of input signals received from the sensors, $\mathbf{u}_k$ is the vector of output signals sent to the actuators, $\mathbf{x}_{est,k}$ is the vector of "current" internal state variables, and $\mathbf{x}_{est,k+1}$ is the vector of "updated" internal state variables. The **F11**, **F12**, **F21**, and **F22** submatrices are user-specified and determine the type of control-estimation-filtering being applied.

The matrix operation above was designed to implement multivariable modern control with state estimation (Ref. 64). For MFDRF and LQDRF control laws, applied to the grid structure , a 5 x 5 submatrix of **F11** represented the matrix **D** of Eq. (4.30), and all other elements of the 48 x 48 coefficient matrix were zero. For the Beam Cross-Cable structure, a 3 x 3 submatrix of **F11** was used to implement MFDRF and LQDRF control. These control laws were implemented

at the maximum sampling rate of 2000 samples per second on both test structures, closely approximating continuous time operation.

LQG control requires the use of portions of the **F21**, **F12**, and **F22** submatrices but not the **F11** submatrix. The LQG control law must be converted to a discrete time design to be implemented by the PC-1000. This conversion process involves integration of the observer equations over one sample period, resulting in a discrete system of the form of Eq. (5.1). The states reconstructed by the observer $\mathbf{x}_{est,k+1}$ of reduced order $2n_R x1$, and the control output $\mathbf{u}_k$, are determined by

$$\mathbf{F12} = -\mathbf{F}_R \tag{5.2}$$

$$\mathbf{F21} = (e^{\tilde{\mathbf{A}}_R \Delta t} - \mathbf{I})\tilde{\mathbf{A}}_R^{-1}\mathbf{K}_R \tag{5.3}$$

$$\mathbf{F22} = e^{\tilde{\mathbf{A}}_R \Delta t} \tag{5.4}$$

where

$$\tilde{\mathbf{A}}_R = \mathbf{A}_R - \mathbf{B}_R\mathbf{F}_R - \mathbf{K}_R\mathbf{C}_R \tag{5.5}$$

The **FIJ** of Eqs. (5.2) - (5.5) occupy appropriate portions of the **FIJ** defined in Eq. (5.1).

Due to a combination of software and hardware problems with the digital controller, the LQG controller could not be implemented on the grid structure in exact manner just described. The number of non-zero elements downloaded to the PC-1000 had to be reduced by a similarity transformation that converts the

$\tilde{\mathbf{A}}_R$ matrix to a block diagonal form. (The matrices needed to implement LQG control on the Beam Cross-Cable structure were small enough to be downloaded to the PC-1000 without this transformation.) This transformation involves using the complex eigenvectors $\tilde{\mathbf{\Phi}}$ of the $\tilde{\mathbf{A}}_R$ matrix to perform the similarity transformation on the matrix. The transformation matrix $\mathbf{T}(n,xn_r)$ consists of the real part of each eigenvector in one column followed by the imaginary part of the same eigenvector in the next column.

$$\mathbf{T} = [real(\tilde{\mathbf{\Phi}}_i), imag(\tilde{\mathbf{\Phi}}_i), ...] \quad i = 1,...,12 \tag{5.6}$$

The similarity transformation is a coordinate transformation relating $\mathbf{x}'_{est}$, the transformed state variable, to $\mathbf{x}_{est}$, the estimated state variable, using $\mathbf{T}$.

$$\mathbf{x}_{est} = \mathbf{T}\mathbf{x}'_{est} \tag{5.7}$$

The continuous time estimator is

$$\dot{\mathbf{x}}_{est} = \tilde{\mathbf{A}}_R\mathbf{x}_{est} + \mathbf{K}_R\mathbf{y}. \tag{5.8}$$

Substituting for $\mathbf{x}_{est}$ and pre-multiplying by $\mathbf{T}^{-1}$ we arrive at

$$\dot{\mathbf{x}}'_{est} = \mathbf{T}^{-1}\tilde{\mathbf{A}}_R\mathbf{T}\mathbf{x}'_{est} + \mathbf{T}^{-1}\mathbf{K}_R\mathbf{y} \tag{5.9}$$

The feedback equation is then

$$\mathbf{u} = -\mathbf{F}_R\mathbf{T}\mathbf{x}'_{est} \tag{5.10}$$

These transformed equations must then be converted to discrete time

$$\mathbf{F21} = (e^{\mathbf{T}^{-1}\tilde{\mathbf{A}}_R\mathbf{T}\Delta t} - \mathbf{I}_R)(\mathbf{T}^{-1}\tilde{\mathbf{A}}_R\mathbf{T})^{-1}\mathbf{T}^{-1}\mathbf{K}_R \tag{5.11}$$

$$\mathbf{F22} = e^{\mathbf{T}^{-1}\tilde{\mathbf{A}}_R\mathbf{T}\Delta t} \tag{5.12}$$

$$\mathbf{F12} = -\mathbf{T}\mathbf{F}_R \tag{5.13}$$

The number of nonzero terms in the transformed matrices is 288 as compared to 816 in the untransformed equations on the grid structure.

Eqs. (5.11) and (5.12) were obtained by integrating the continuous time equation (Eq. 5.9) across one time step, t_n to t_{n+1}. A Pade expansion was used to evaluate the matrix exponential of equations (5.11) and (5.12) at $\Delta t = 0.001$ seconds. Δt was chosen as small as possible subject to machine limitations so as to approximate continuous time as closely as possible. It should be noted that the discretization process does not account for the PC-1000's time delay of 1.35 Δt. This discretization process was checked by determining the roots of the discrete system at a sampling rate of $1/\Delta t = 1000$ samples per second in the z-plane, transforming them to the s-plane with the transformation (Ref. 65)

$$z = e^{s\Delta t} \tag{5.13}$$

The control signals $\mathbf{u}_k$ generated by the PC-1000 were filtered by single-stage passive RC low-pass filters (corner frequency, 677 Hz). These filters were primarily smoothing filters present to eliminate the stairstep nature of the output signal from the PC-1000's zero-order hold digital-to-analog converter. Each

control signal finally passed into a controlled-current power amplifier, which produced a current proportional to the input voltage to drive the actuator.

Figure 21 is a schematic diagram of the control loop with the Data Acquisition and Analysis unit shown to the side. The velocity sensors produce a voltage proportional to the velocity of the structure at that point. This voltage goes to the high input impedence operational amplifier and then to both the PC-1000 and the data acquisition box. The PC-1000 performs the calculations for the type of control being implemented and outputs a voltage as the control signal. The control signal is filtered by a passive low pass filter with a relatively high cutoff frequency (677 Hz) to smooth out the stairstep nature of the signal from the PC-1000. Then the controlled current power amplifiers take the voltage signal and produce a proportional current to be applied to the forcing coils. Notice also the excitation signal added to one of the control signals before the control signal enters the power amplifier. This control loop is typical for both the Beam-Cross-Cable structure and the Hanging Grid structure.

5.4 Data Acquisition and Analysis

An STI-11/23 data acquisition and analysis system developed by Synergistic Technology Inc. was the system used to collect the experimental data. The same system also generated excitation signals, received measurement sensor signals, and performed all data analysis. The excitation signal was added to a control

feedback signal for one of the controllers so that one actuator served the dual purpose of control actuator and exciter.

5.4.1 Mode Shape Testing

Modal tests were performed on the hanging grid structure to determine mode shapes and natural frequencies. Velocity data was obtained on the aluminum grid at the twelve lower joints. Displacement data was also taken on the bottom sides of the large aluminum plates at the ends of the top beams. The displacement data was then divided by the distance to the rotational axis of the top beam producing data in the rotational DOF at that point. The voltage forcing the structure at joint 4 was also measured. Two types of excitation were applied at this point - a broadband pseudo-random function and an incremental sine sweep function. The broadband excitation produced data from 0 to 10 Hz while the incremental sine sweep could be focused on narrower frequency bands for information on specific modes. Primarily data was gathered with incremental sine sweep data with spot checking through broadband random excitation. For a structure as complex as the hanging grid neither of these excitation methods is best for mode shape testing. The best method is to use sine dwell techniques with multiple point excitation to accurately identify the peak frequency and shake out the pure mode shape.

The forcing signals were set as high as possible consistent with maintaining linear behavior of the velocity sensors and force actuators. Fast Fourier trans-

forms (FFTs) of the response and excitation signals were calculated and the former divided by the latter producing either Velocity Frequency Response Functions (VFRFs) or Displacement Frequency Response Functions (DFRFs). The VFRFs were then integrated in the frequency domain. Peak levels and phases were then determined at each natural frequency for each response point. This peak level data is the raw mode shape data. The raw mode shape data was then normalized to the maximum number for each mode (maximum deflection in each mode = 1). Cubic splines were calculated for each diagonal and horizontal aluminum bar and plotted in Figures 6 through 16 in Chapter 2. Data was not taken along the length of the top beam which is why top beam bending is not evident in mode 7 (Fig. 12).

5.4.2 Control System Testing

Testing of the control system required only the implementation of the control loop in addition to the testing procedure for the modal test. One major step that must not be skipped in either modal testing or controller testing is the order in which the various pieces of electrical equipment are turned on. The two computer systems must be turned on and the application software brought on-line before any of the sensors or actuators are turned on. The computers must be turned on first because the relatively large starting transients produced by the computer systems can cause large impulses to be applied to the structure if the actuators are on. Next the PC-1000 must be running before the actuators or

sensors are on because when the PC-1000 is on and the control is not, large DC signals are put out by the PC-1000. This can cause the force coils to overheat or burn. Now the power amplifiers force coils may be turned on and lastly the power supply for the operational amplifiers may be turned on. The power supply for the operational amplifiers must be last because the operational amplifiers operating at a unit gain are relatively unstable and will destabilize and produce large levels of electronic noise if any electrical equipment is switched on around them after they are on.

After all equipment is switched on, the test procedure is the same as for the modal tests. For the tests on the Beam-Cross-Cable, displacement was gathered for the controlled system at grid point 6 due to excitation at grid point 9 (Fig. 2). On the hanging grid structure, velocity data was gathered at joints 1,2,3,4,5, and 8 due to force at joint 4 (Fig. 5).

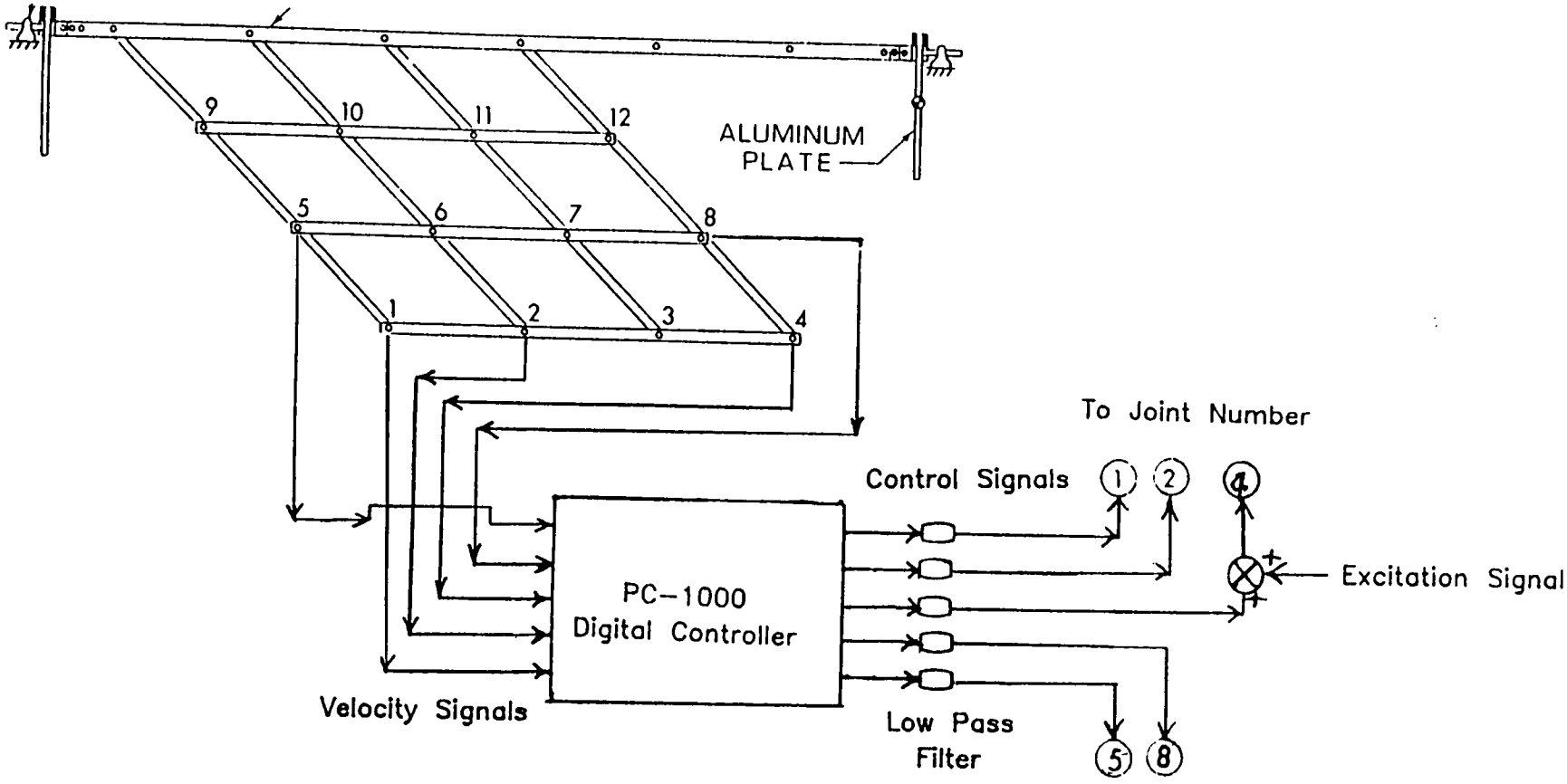

Figure 21. Schematic Diagram of Control Loop

Chapter 6

Comparison of Closed-Loop Analytical and Experimental Results

6.1 Comparison of Analytical and Experimental Controlled System Results for the Beam Cross-Cable Structure

The two DRF control systems (MFDRF and LQDRF) designed for the Beam Cross-Cable structure were required to produce at least 3% damping in the first six modes of the structure. The optimization problems of Equations (4.32) and (4.38) were solved by using NEWSUMT-A. The optimization procedure produced the gain matrices shown in Table 7 for MFDRF and LQDRF control.

Notice that MFDRF control is only coupled between two of the three sensor/actuator pairs and that LQDRF control is fully coupled. LQR control achieved 3% damping with **Q** and **R** matrices of **I** and 0.22 **I** respectively. The Kalman filter was obtained for $\mathbf{V}_1 = 10^{-6}\mathbf{I}$, $\mathbf{V}_2 = 5x10^{-4}\mathbf{I}$ and $\alpha = 0.2$. Table 8 lists the closed loop damping ratios for the LQR, the reduced model LQG, and the two DRF control designs. In this table notice that MFDRF control produces three modes with damping ratios near the three percent lower limit and otherwise generally lower damping than LQDRF or LQG control. The sixth damping ratio produced by LQG control is less than 3% because of model reduction and state estimation. Table 9 presents the quadratic performance indices of LQR, LQG, MFDRF, and LQDRF control designed with the full model. (The effect of model reduction on the performance indices was found to be minimal.) The deterioration in the performance of the higher frequency modes due to the need for estimation is clearly shown by the LQR and LQG columns. Due to this loss of performance, the DRF control laws have better performance indices than LQG control in the higher modes.

Representative DFRF magnitudes, for the open loop system and the closed loop system using MFDRF, LQDRF, and LQG control laws, are plotted in Figure 22 (A, C, E, and G) for experimental measurements at grid point 6 with excitation at grid point 9. The corresponding analytical results for the full order model are plotted in Fig. 22 (B, D, F, and H). (For a complete description of the analytical results for the Beam Cross-Cable structure see Reference 59.) The open loop analytical results and measurements (Fig. 22 A and B) verify the na-

tural frequencies of the theoretical model (i.e. 1.9 Hz, 4.8 Hz, and so on), show realistic modeling of structural damping (which was based on experimental measurements). Table 10 lists the ratios of theoretical peak levels to experimental peak levels for the open loop and the three controlled cases. From these numbers, it can be seen that even though the frequencies and peak shapes compare well there may be significant differences in the actual peak levels. Modes 1,2,4, and 5 are significantly lower for the open loop system in the analytical DFRFs. A probable cause of this is the extremely low inherent damping in the structure and the frequency spacing of the evaluation points. The peaks are so sharp that a minor shift away from the actual resonant frequency causes a large decrease in the peak level. Good agreement between analysis and experiment is observed for all three controlled systems. In these cases, the agreement includes the frequency location, shape of the DFRF and the peak level ratios. For the controlled systems the damping is increased enough so that a small shift in frequency does not significantly affect the peak levels. The worst agreement in the peak levels for the controlled systems occurred with LQG control. This may be due to the complexity of LQG control and its need for a full state observer which the DRF controls do not need.

Considering all aspects of the analytical and experimental results, we have seen that the DRF control designs have comparable performance indices, produce more damping in the uncontrolled modes, are unconditionally stable, and have better experimental/analytical correlation than the LQG control design.

The controlled system was well behaved for MFDRF and LQDRF control with no unexplained phenomena observed. This was also true for LQG control with one notable exception. When the system was allowed to rest with the control on for two or three minutes, a limit cycle at approximately 41 Hz developed. This limit cycle would grow until it reached a moderately low level and then remain at that level despite additional excitation. The vibration could be easily stopped by hand, but would appear again after the same two or three minutes. The most probable cause for this behavior is the time delay of the feedback signal through the PC-1000. This time delay causes a phase shift of the output signal which when coupled with the proximity of a structural vibration mode could cause the limit cycle.

6.2 Comparison of Control Systems - Analytical Results for the Hanging Grid Structure

The control system includes five force actuators, (Ref. 63) each colocated with a velocity sensor (i.e. $n_c = n_s = 5$) at joints 1, 2, 4, 5, and 8. Analytical results from controllers designed based on the finite element exact reduced model are presented first and the results from the corrected Guyan reduced model later in this section. Because the aim of the DRF control system is to achieve simplicity and robustness, a simplified LQDRF design was also considered. This design is

limited to a diagonal matrix **D** so that the controllers are uncoupled, with each controller constituting in effect an electric dashpot.

6.2.1 Exact Reduction Results

The LQR control system was designed with $\mathbf{Q} = 0.01\mathbf{I}$ and $\mathbf{R} = 0.84\mathbf{I}$, selected to achieve a minimum of 3 percent damping in the first five (n_m) vibration modes. The LQDRF design used the same **Q** and **R** matrices and the same stability margins imposed on the first n_m vibration modes. Both full and diagonal feedback matrices were calculated for LQDRF control. Initial conditions in the form of the first $n_f = 5$ mode shapes were used for the minimization routine.

The MFDRF controller was designed with the same stability margins (n_m = 5, ζ_L = 0.03). Table 11 displays the three direct rate feedback designs (i.e. matrix **D**) produced. The gains in the LQDRF designs are generally larger than the gains for the MFDRF design and the LQDRF controller uses the third sensor/actuator pair where the MFDRF controller has a zero feedback gain for that position. This indicates that for MFDRF control the optimizer determined that this actuator/sensor position was ineffective in controlling the desired modes.

The Kalman filter was designed with alpha shift ($\alpha = .05$) and noise matrices ($\mathbf{V}_1 = 10^{-10}\mathbf{I}$, $\mathbf{V}_2 = .5\mathbf{I}$) selected to make the real parts of the filter poles about three times larger than the real parts of the regulator poles. The alpha shift dominated the design, while the noise matrices had an insignificant influence.

Table 12 contains the damping ratios for the three DRF designs as well as for the LQG controller designed with the reduced model applied to both the reduced model and the full model, (obtained from the eigenvalues of $\mathbf{A}_E$, Eq. (4.24)) and open loop damping ratios. Comparing the two LQG columns, it is seen for the first five controlled modes that the model reduction has little effect on the damping ratios. Similarly, applying the DRF control laws designed with the reduced model to the full model produced only minor differences in the third significant figure of the damping ratios and performance indices.

Quadratic performance indices (using $\mathbf{Q} = 0.01\mathbf{I}, \mathbf{R} = 0.84\mathbf{I}$) were calculated (see Eqs. (4.20) and (4.26)) for initial conditions in the form of the first twelve open loop mode shapes, and results are presented in Table 13. Comparison of the full model LQR and LQG columns shows that the deterioration in performance due to the need for an observer is significant in all modes. Model reduction effects on the performance indices are minimal as is displayed by the small increases in the indices when the reduced model controller is applied to the full model. The reduced model LQG design applied to the full model performs better than the DRF designs for the lowest two modes and modes 7 through 12. The DRF designs perform better in modes 3 through 6 with some exceptions. Overall, it appears that for the 5 modes used in the LQDRF design its performance is comparable or better than the LQG design. That is, the losses due to suboptimality of the LQDRF design are smaller than the losses of the LQG performance due to the need for an observer. To improve the performance of the higher frequency modes with diagonal LQDRF control, the performance of all

12 modes were included in the optimization. Since the higher frequency modes typically have performance indices 10 or more times higher than the first few modes, a variation on the objective function was used. Each performance index from the LQDRF design was divided by the corresponding performance index from LQR control so that the best ratio possible was one. The ratios were then required to be less than the objective function. This variation was needed to prevent the optimizer from lowering the highest performance index at the expense of the lower values. The last column in Table 13 presents the performance indices obtained with this last formulation. Some modes, the first, second and eleventh, suffered a slight increase in their performance indices but on the whole significant improvements were made making the simple and robust diagonal LQDRF design even more competitive with LQG control.

Comparison of the three direct rate feedback laws shows that LQDRF is better than MFDRF control for the first five modes and that the diagonal LQDRF controller has the best performance of the DRF designs in modes 1 and 2. Above the fifth mode, MFDRF control has better performance. The superior performance of the LQDRF design for the first 5 modes is a direct result of the different objective function of the MFDRF controller.

Spillover effects from applying a controller designed with a reduced model to the full model were present in three of the modes not included in the reduced model. We assumed that these modes had 1% damping in the open loop model, and when the reduced model LQG controller was applied to the full model modes 25, 26, and 33 were partially destabilized. The direct rate feedback control laws

increased the damping in all modes up to number 45 and did not affect the rest of the modes.

To determine the effects the form of the **Q** matrix has on the performance of the controlled systems, we selected a different **Q** matrix and calculated LQR, LQG, and diagonal LQDRF controllers. The **Q** matrix selected was

$$\mathbf{Q} = \begin{bmatrix} \mathbf{M} & \mathbf{0} \\ \mathbf{0} & \mathbf{K} \end{bmatrix} \tag{6.1}$$

which relates the $\mathbf{x}^T\mathbf{Q}\mathbf{x}$ to the total energy of the structure. The **R** matrix needed to produce a minimum damping ratio of 0.03 in the first five modes was $\mathbf{R} = 7.5x10^5\mathbf{I}$. The same noise covariance matrices were used to calculate the Kalman filter for LQG control. Performance indices for the three new control designs are listed in Table 14. Comparing these values, we notice the same behavior that was present for the previous controllers. The direct rate feedback design does not match the performance of the LQG controller for the first two modes but it does for the next three modes and then for the higher modes the DRF design again does not match the LQG design. This indicates that the general behavior of the performance indices is not dependent on the selection of the weighting matrices.

6.2.2 Corrected Guyan Reduced Model Results

Controllers designed with the corrected reduced model were similar to the controllers just described with some significant differences. Table 15 shows the feedback matrices for these designs. The MFDRF controller again is primarily a diagonal matrix but all of the diagonal terms are non-zero and their values are about half of the previous design. This design uses about 40% less control force than the analytic reduction MFDRF design. The new LQDRF controller is also quite different. It has larger diagonal terms on 3 of 5 elements and has larger off-diagonal terms indicating heavier coupling. The off-diagonal terms are as large as the smallest of the diagonal terms. Diagonal LQDRF control designed with the corrected Guyan model uses about half the control force as the exact reduction design. LQR control required $\mathbf{Q} = 0.01\mathbf{I}$ and $\mathbf{R} = 1.387\mathbf{I}$ to produce a minimum damping ratio of 0.03 in the first five modes. Table 16 contains the damping ratios that these new controller designs produced. Comparing these damping ratios with the damping ratios in Table 9 it is evident that that the new controllers produce significantly different results. The new MFDRF and LQDRF designs each have two modes at the lower damping ratio limit (ζ_L = 0.03) and generally lower values for the rest of the modes. The LQG control has damping ratios that are both significantly higher and lower than the previous design. Performance indices displayed the same trends for this model as they did for the previous model. The DRF designs were better in the intermediate modes and LQG control was better in the lowest and highest frequency modes.

6.2.3 Application of Exact Reduced Model Controllers to Corrected Guyan Model

The LQG, MFDRF, and diagonal LQDRF controllers designed with the exact reduced model were applied to the corrected Guyan reduced model for checking the robustness properties of these controllers. Table 17 presents the damping ratios for these three controllers applied to the exact reduced model and then to the corrected Guyan reduced model. For LQG control, the most significant changes in the damping ratios occur in modes 2 and 6 where the damping ratios are reduced by an order of magnitude when control was applied to the corrected Guyan model. The damping ratios of the other modes change up to 75 percent both gaining and losing damping. MFDRF control applied to the corrected Guyan model is more robust gaining an order of magnitude of damping in mode 7 and having a largest reduction of 75 percent in damping in mode 2. Diagonal LQDRF control is the most robust with similar behavior to the MFDRF control. It also gains an order of magnitude of damping in mode 7 and has the greatest reduction (53 percent) in mode 2.

The performance indices calculated from applying the exact reduced model controllers to the corrected Guyan model are of course different from the performance indices obtained from applying the controllers to the exact reduced model simply because the two models are different. Table 18 lists these performance indices along with the previuosly obtained indices from applying the exact reduction controllers to the exact reduction. The performance of the LQG

and LQDRF controllers is now similar, with the LQG controller having the lowest performance indices for modes 1, 2, 9-12, the LQDRF controller for modes 3-8. The Mfdrf controller is also better than the LQG controller for modes 4-8. Overall Table 18 shows that when modeling errors are accounted for the difference in performance between the LQG controll and the DRF controllers tend to become less predictable.

6.3 Comparison of Analytical and Experimental Results for the Hanging Grid Structure

6.3.1 Open Loop Results - Analytical and Experimental

Figure 23 presents open loop analytical VFRFs for both of the reduced models along with the experimental VFRF. (Input and output both at joint 4 on the grid.) The frequency range of interest is 0 to 10 Hz which includes all of the modes retained in the reduced models. Note that the vertical scale is logrithmic from .1 to 1000 inch-per-second per pound (IPS/LB). Looking at the first three modes of the structure, the corrected Guyan model is seen to be more accurate in its prediction of the peak levels than the exact reduction as well as matching the experimental frequency. (The corrected model will always match the open loop frequency.)

Table 19 lists the analytical to experimental peak level ratios for the first 4 modes of the open loop structure. (The first five modes were of primary interest but the fifth mode does not show up well enough to get a good peak level from the experimental data.) A number greater than one indicates that the analysis predicts a higher peak than was actually found and a number less than one indicates a lower peak was predicted. Notice that for modes 1 and 3 the corrected Guyan model is more accurate and for modes 2 and 4 the exact reduced model is more accurate. The last row of the table is the average of the absolute value of one minus the peak ratio giving an average error for the first four modes. This number indicates that the corrected Guyan model is better than the exact reduced model for these modes. Mode 5 is just visible in the experimental VFRF, visible in the corrected Guyan VFRF, and not visible at all in the exact reduction. Qualitatively, the corrected Guyan model looks better for modes 6 - 8 and the exact reduction better for modes 9 - 12.

6.3.2 Exact Reduction Control System Results - Analytical and Experimental

Representative VFRF magnitudes are presented in Figure 24 for the analytical and experimental closed-loop system with MFDRF control. The first VFRF is MFDRF control applied to the Exact reduction. Next, is the plot of the experimental results and last, is MFDRF control applied to the corrected Guyan reduced model. Figure 25 is the same set of plots for LQDRF control, Figure 26

for diagonal LQDRF control, and Figure 27 for LQG control. Table 20 lists the analytical to experimental peak level ratios for the four control systems.

Each of the closed loop VFRFs exhibit many of the same characteristics. The VFRFs obtained from applying control to the corrected Guyan model qualitatively better match the experimental results than the VFRFs obtained by applying control to the exact reduction for modes 1 through 5. The exact reduction provides a better match for modes 9 through 12 and with the exception of LQG control, the two models are about equal for modes 6 through 8. Applying LQG control designed with the exact reduced model to the corrected Guyan model produces a partial destabilization of mode 6 in the analytical results that is not apparent in the experimental results.

The very good analytical-experimental agreement of the diagonal LQDRF design demonstrates the advantage of working with a simple and robust control system.

6.3.3 Corrected Guyan Reduction Control System Results - Analytical and Experimental

Since the VFRFs from the Exact reduced controller applied to the corrected Guyan model predicted the experimental results more accurately for the first five modes, we calculated new controllers based on the corrected Guyan model (see discussion in section 6.2.2) and then compared experiment and theory. Representative analytical and experimental VFRF magnitudes are presented in Figure

28 for MFDRF control, Figure 29 for LQDRF control, Figure 30 for diagonal LQDRF control, and Figure 31 for LQG control. As with the controllers designed with the exact reduced model, the analytical VFRFs agree qualitatively with the experimental VFRFs for modes 1 through 8 but do not match well for modes 9 to 12. Table 21 lists the analytical to experimental peak level ratios for these control systems. The level of agreement between the experiment and analysis is dependent on the control being implemented. LQG control predicted consistently low peak levels while both of the direct rate feedback controls predicted peaks that were both higher and lower than the experimental peaks. MFDRF control had the lowest average error and LQDRF control had the highest.

The controllers designed with the corrected Guyan model applied to the corrected Guyan model had lower errors with LQG and MFDRF control than the controllers designed with the exact reduction applied to the exact reduction. The corrected Guyan model had better predictions when the exact reduction LQDRF and LQG controllers were applied than the corrected Guyan controllers applied to the corrected Guyan model.

Once again the diagonal LQDRF exhibited very good analytical-experimental match demonstrating the advantage of this design.

Table 7. Gain matrices D for DRF control (lb-s/in) (Beam structure)

Actuator Point No.	MFDRF Control Sensor Point No.		
	5	7	9
5	0.0500	0.0000	0.0000
7	0.0000	0.0359	-0.0139
9	0.0000	-0.0139	0.0222
Actuator Joint No.	LQDRF Control Sensor Joint No.		
	5	7	9
5	0.0581	0.0261	-0.0011
7	0.0261	0.1018	-0.0014
9	-0.0011	-0.0014	0.0448

Table 8. Analytical Closed Loop Damping Ratios for the Beam Cross-Cable Structure

Mode	MFDRF	LQDRF	LQG
1	0.1830	0.5589	0.6216
2	0.0304	0.0695	0.2270
3	0.0600	0.1151	0.1437
4	0.0301	0.0428	0.0666
5	0.0454	0.0613	0.0563
6	0.0300	0.0300	0.0298

Table 9. Analytical Closed Loop Performance Indices for the Beam Cross-Cable Structure

Mode	LQR	LQG	MFDRF	LQDRF
1	43.	56.	97.	63.
2	39.	44.	144.	72.
3	27.	34.	45.	32.
4	38.	48.	57.	46.
5	62.	78.	65.	68.
6	108.	145.	113.	110.

Table 10. Analytical/Experimental Peak Level Ratios for the Beam Cross-Cable Structure

Mode	Open Loop	MFDRF	LQDRF	LQG
1	0.55	1.02	0.89	1.00
2	0.17	0.85	0.84	1.05
3	1.00	1.00	1.00	1.07
4	0.50	1.04	1.17	0.51
5	0.35	0.78	0.69	0.68
6	1.00	0.97	0.88	0.55
Avg. Error	0.41	0.08	0.15	0.22

Excitation at Grid Point 9. Response at Grid Point 6.

Table 11. Gain matrices D for DRF control (lb-s/in) (Exact reduced model) - Hanging Grid

Actuator Joint No.	MFDRF Control Sensor Joint No.				
	1	2	4	5	8
1	0.0050	0.0001	0.0000	-0.0001	-0.0001
2	0.0001	0.0060	0.0000	-0.0001	0.0000
4	0.0000	0.0000	0.0000	0.0000	0.0000
5	-0.0001	-0.0001	0.0000	0.0055	0.0001
8	-0.0001	0.0000	0.0000	0.0001	0.0058
Actuator Joint No.	LQDRF Control (n_f = 5, Q = 0.01 I, R = 0.84 I) Sensor Joint No.				
	1	2	4	5	8
1	0.0102	-0.0012	-0.0020	0.0010	-0.0002
2	-0.0012	0.0068	-0.0002	0.0004	0.0000
4	-0.0020	-0.0002	0.0050	0.0000	-0.0018
5	0.0010	0.0004	0.0000	0.0077	-0.0005
8	-0.0002	0.0000	-0.0018	-0.0005	0.0062

Diagonal LQDRF control

diag(.0062, .0058, .0096, .0057, .0061)

Table 12. Theoretical Open and Closed Loop Damping Ratios from Exact Reduction - Hanging Grid

Mode No.	LQG	LQG Applied to Full-model	MFDRF	LQDRF	Diagonal LQDRF	Open Loop
1	0.1177	0.1176	0.1272	0.1556	0.3094	0.044
2	0.5315	0.5298	0.0518	0.0940	0.1275	0.029
3	0.2318	0.2317	0.1045	0.1863	0.1435	0.028
4	0.0514	0.0514	0.0325	0.0634	0.0742	0.012
5	0.0299	0.0300	0.0300	0.0300	0.0301	0.006

Table 13. Quadratic Performance Index (Q = 0.01 I, R = 0.84I) - Exact Reduction Hanging Grid

Initial Conditions	Full-Model Controller		Reduced Model Applied to Full Model
Mode No.	LQR	LQG	LQG
1	0.617	0.766	0.778
2	0.553	0.586	0.589
3	0.682	1.011	1.012
4	1.077	1.427	1.431
5	3.926	4.558	4.570
6	2.175	2.820	2.734
7	10.787	11.123	11.195
8	13.223	13.777	13.737
9	3.561	4.122	4.128
10	7.266	7.692	7.742
11	4.837	5.218	5.224
12	3.742	3.979	4.033

	Reduced-Model Controllers					12 P.I.
					Diagonal	Diagonal
	LQR	LQG	MFDRF	LQDRF	LQDRF	LQDRF
1	0.622	0.777	1.629	1.375	0.956	1.063
2	0.554	0.588	1.603	0.905	0.779	0.849
3	0.685	1.011	0.948	0.752	0.787	0.789
4	1.073	1.427	1.441	1.218	1.284	1.113
5	3.908	4.550	4.007	3.939	3.924	3.952
6	2.162	2.723	2.457	3.524	2.590	2.533
7	6.917	7.273	10.867	31.710	12.205	11.821
8	12.956	13.469	16.212	31.256	33.699	22.145
9	3.545	4.113	4.639	4.762	5.028	4.000
10	7.232	7.710	8.820	13.456	9.045	9.300
11	4.809	5.197	7.327	12.652	7.635	8.219
12	3.693	3.888	4.788	6.046	7.005	5.164

Table 14. Quadratic Performance Index for Mass and Stiffness Based Q Matrix and R = 750000 I

Initial Conditions Mode No.	Reduced Model Controllers (Performance Indices $x10^5$) LQR	LQG	Diag. LQDRF
1	1.39	1.48	1.68
2	1.95	2.02	2.54
3	2.11	3.80	2.76
4	10.25	14.17	12.67
5	38.75	49.53	50.58
6	35.97	39.16	40.91
7	26.12	30.74	186.20
8	279.00	283.00	325.20
9	75.31	82.33	85.14
10	307.70	326.30	390.60
11	303.70	335.00	370.40
12	61.66	65.59	68.340

Table 15. Gain matrices D for DRF control (lb-s/in) (Corrected Guyan reduced model) - Hanging Grid

Actuator Joint No.	MFDRF Control Sensor Joint No.				
	1	2	4	5	8
1	0.0026	0.0000	-0.0000	-0.0000	-0.0000
2	0.0000	0.0029	0.0000	-0.0000	-0.0000
4	-0.0000	0.0000	0.0035	-0.0000	-0.0000
5	-0.0000	-0.0000	-0.0000	0.0029	0.0000
8	-0.0000	-0.0000	-0.0000	0.0000	0.0027

Actuator Joint No.	LQDRF Control (n_f = 5, Q = 0.01 I, R = 1.387 I) Sensor Joint No.				
	1	2	4	5	8
1	0.0086	-0.0032	-0.0050	0.0068	0.0037
2	-0.0032	0.0081	-0.0000	0.0046	-0.0010
4	-0.0050	-0.0000	0.0094	-0.0047	-0.0045
5	0.0068	0.0046	-0.0047	0.0097	0.0034
8	0.0037	-0.0010	-0.0045	0.0034	0.0045

Diagonal LQDRF control
diag(.0030, .0030, .0042, .0031, .0031)

Table 16. Analytical Closed Loop Damping Ratios from Corrected Guyan Model Designs Hanging Grid

Mode No.	LQG	MFDRF	LQDRF	Diagonal LQDRF
1	0.3572	0.0822	0.0979	0.0979
2	0.0741	0.0300	0.0736	0.0335
3	0.1582	0.0575	0.2740	0.0704
4	0.3917	0.0332	0.0301	0.0389
5	0.0300	0.0300	0.0300	0.0309

Table 17. Closed Loop Damping Ratios from Exact Reduction Controllers Applied to the Corrected Guyan Model

Mode No.	LQG EA	LQG CG	MFDRF EA	MFDRF CG	Diagonal LQDRF EA	Diagonal LQDRF CG
1	0.1177	0.2356	0.1272	0.0835	0.3094	0.1780
2	0.5315	0.0468	0.0518	0.0129	0.1275	0.0601
3	0.2318	0.2102	0.1045	0.0651	0.1435	0.1299
4	0.0514	0.0445	0.0325	0.0329	0.0742	0.0752
5	0.0299	0.0447	0.0300	0.0471	0.0301	0.0471
6	0.0192	0.0021	0.0246	0.0371	0.0311	0.0300
7	0.0028	0.0018	0.0038	0.0343	0.0040	0.0279
8	0.0023	0.0057	0.0024	0.0062	0.0030	0.0069
9	0.0117	0.0130	0.0095	0.0109	0.0226	0.0239
10	0.0056	0.0170	0.0083	0.0196	0.0086	0.0294
11	0.0080	0.0146	0.0159	0.0281	0.0167	0.0254
12	0.0056	0.0044	0.0056	0.0060	0.0105	0.0116

EA = Exact reduction controller applied to exact reduction
CG = Exact reduction controller applied to corrected Guyan reduction

Table 18. Quadratic Performance Indices for Exact Reduction Controllers Applied to the Corrected Guyan Model

Mode No.	LQG EA	LQG CG	MFDRF EA	MFDRF CG	Diagonal LQDRF EA	Diagonal LQDRF CG
1	0.777	1.031	1.629	2.653	0.956	1.442
2	0.588	1.432	1.603	6.232	0.779	1.435
3	1.011	1.407	0.948	1.572	0.787	0.910
4	1.427	1.709	1.441	1.695	1.284	1.307
5	4.550	3.244	4.007	2.591	3.924	2.293
6	2.723	21.259	2.457	3.628	2.590	2.795
7	7.273	8.573	10.867	2.354	12.205	1.681
8	13.469	23.408	16.212	7.011	33.699	1.589
9	4.113	3.417	4.639	3.976	5.028	4.209
10	7.710	3.144	8.820	2.940	9.045	4.435
11	5.197	2.190	7.327	5.246	7.635	3.975
12	3.888	4.395	4.788	7.635	7.005	6.780

EA = Exact reduction controller applied to exact reduction
CG = Exact reduction controller applied to corrected Guyan reduction

Table 19. Analytical/Experimental Peak Level Ratios (Open Loop) Hanging Grid

Mode No.	Open Loop E.A.	Open Loop C.G.
1	1.78	1.25
2	0.86	0.72
3	0.55	1.02
4	0.98	1.38
Avg. Error	0.35	0.23

E.A. = Exact Analytical C.G. = Corrected Guyan

Table 20. Analytical/Experimental Peak Level Ratios for Exact Reduction Controller - Hanging Grid

Mode	LQG		MFDRF		LQDRF		Diagonal LQDRF	
No.	E.A.	C.G.	E.A.	C.G.	E.A.	C.G.	E.A.	C.G.
1	0.47	0.99	2.02	1.42	1.61	1.07	1.41	1.23
2	0.35	1.09	0.75	1.32	0.73	0.76	0.92	1.10
3	0.65	0.59	0.55	0.75	0.62	0.66	0.85	0.99
4	0.55	0.66	0.55	0.54	0.63	0.63	0.94	0.90
Avg. Error	0.51	0.22	0.54	0.36	0.41	0.26	0.18	0.11

E.A. = Exact Analytical C.G. = Corrected Guyan

Table 21. Analytical/Experimental Peak Level Ratios for the Corrected Guyan Controllers - Hanging Grid

Mode No.	LQG	MFDRF	LQDRF	Diagonal LQDRF
1	0.93	1.14	1.57	1.24
2	0.73	1.19	0.91	0.99
3	0.46	0.90	0.53	0.97
4	0.68	0.82	0.45	0.91
Avg. Error	0.30	0.15	0.42	0.09

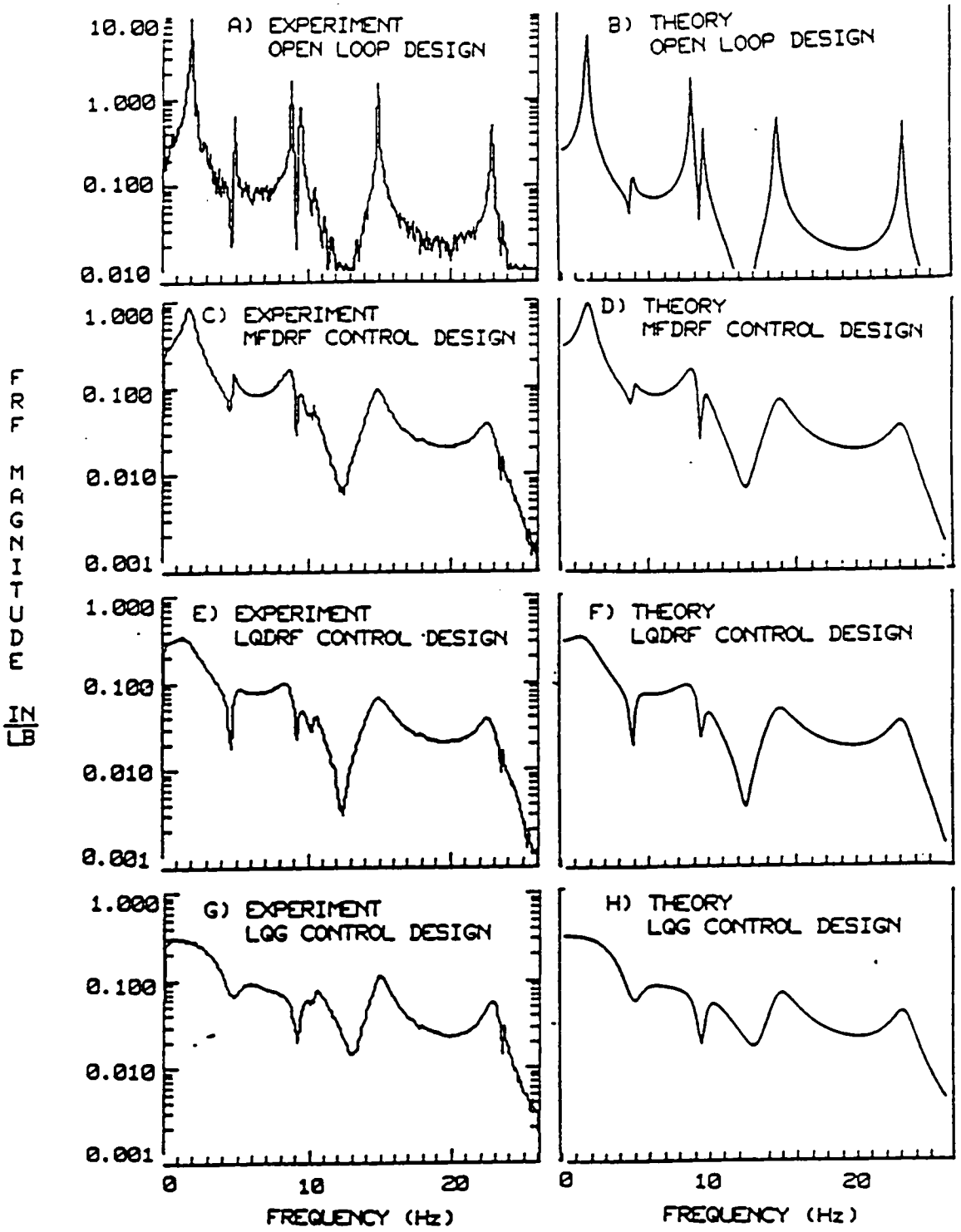

Figure 22. Beam Cross-Cable Displacement Frequency Response Functions for the Controlled Systems

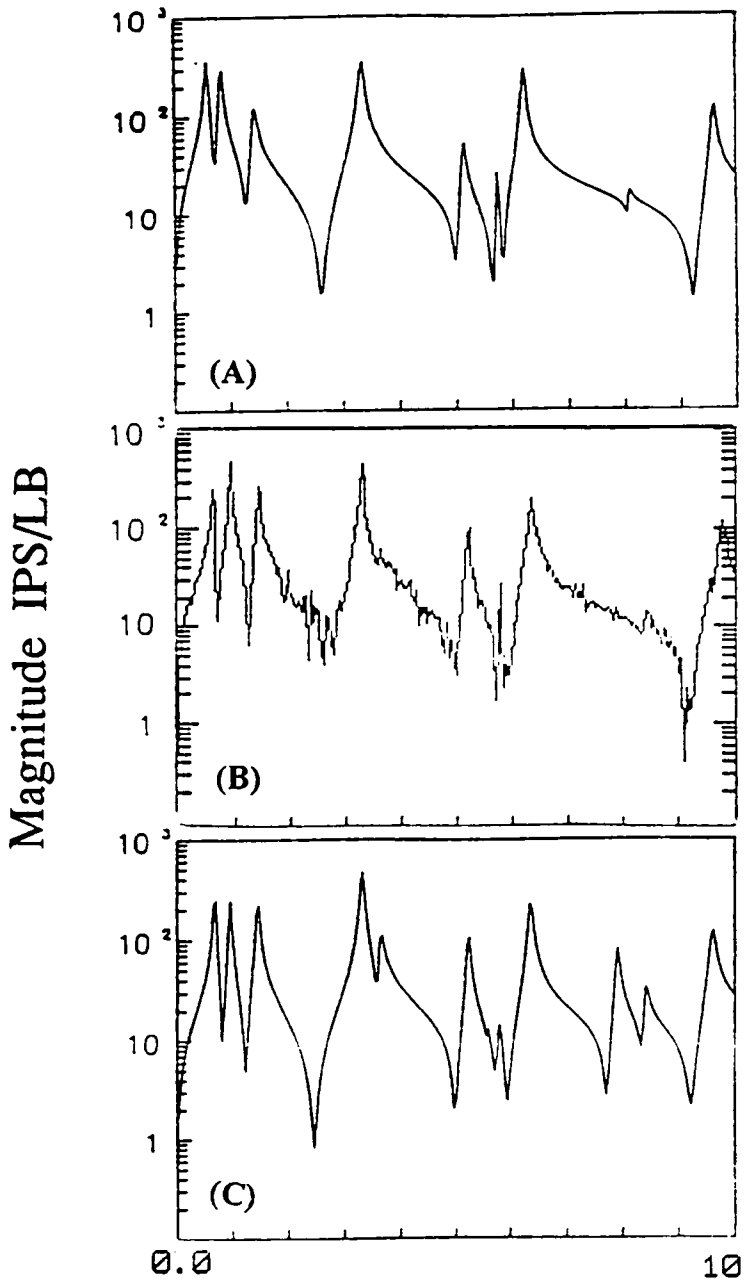

Figure 23. Hanging Grid Velocity Frequency Response Functions for the Open Loop System: (A) Exact reduction, (B) Experimental, (C) Corrected Guyan model

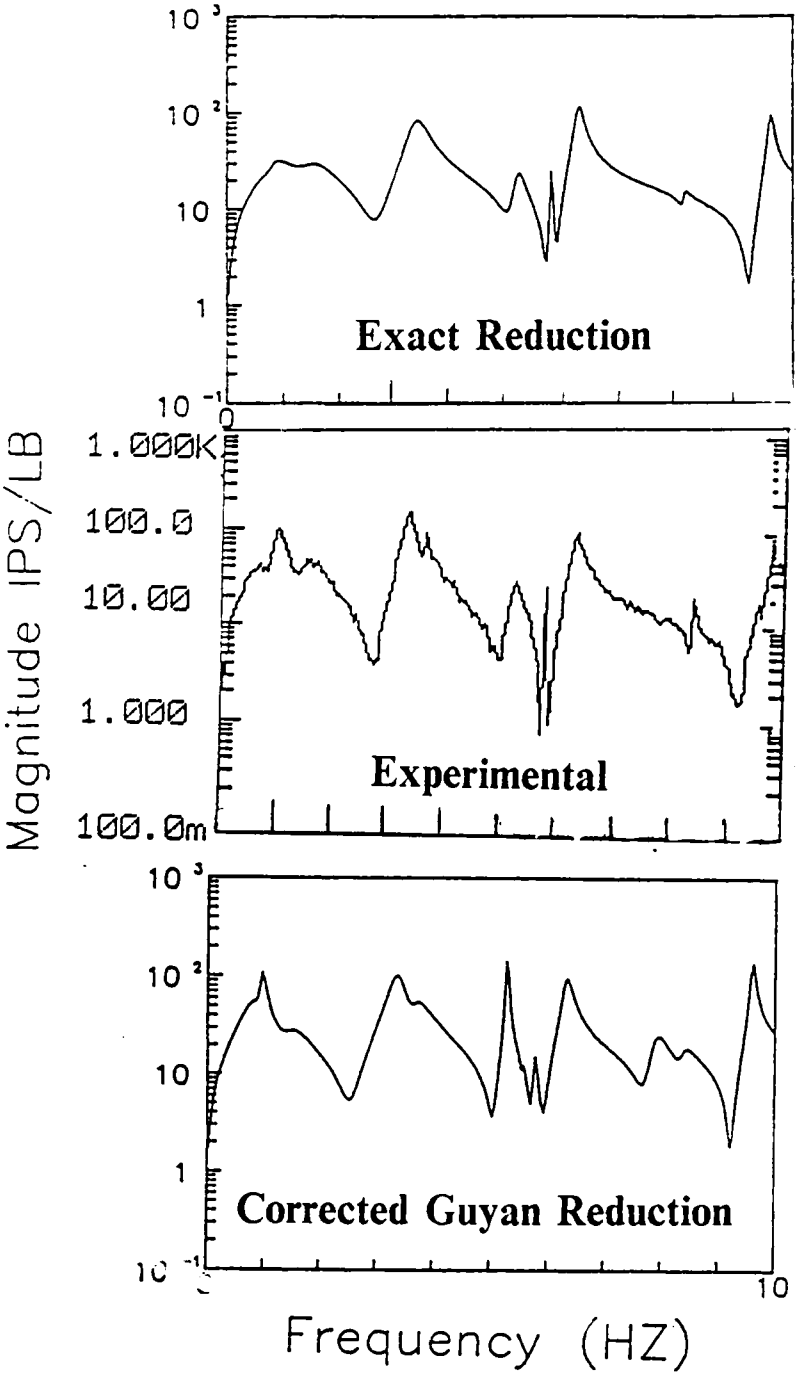

Figure 24. Hanging Grid VFRFs for MFDRF Control on (A) Exact Reduction, (B) Experiment, (C) Corrected Guyan Reduction

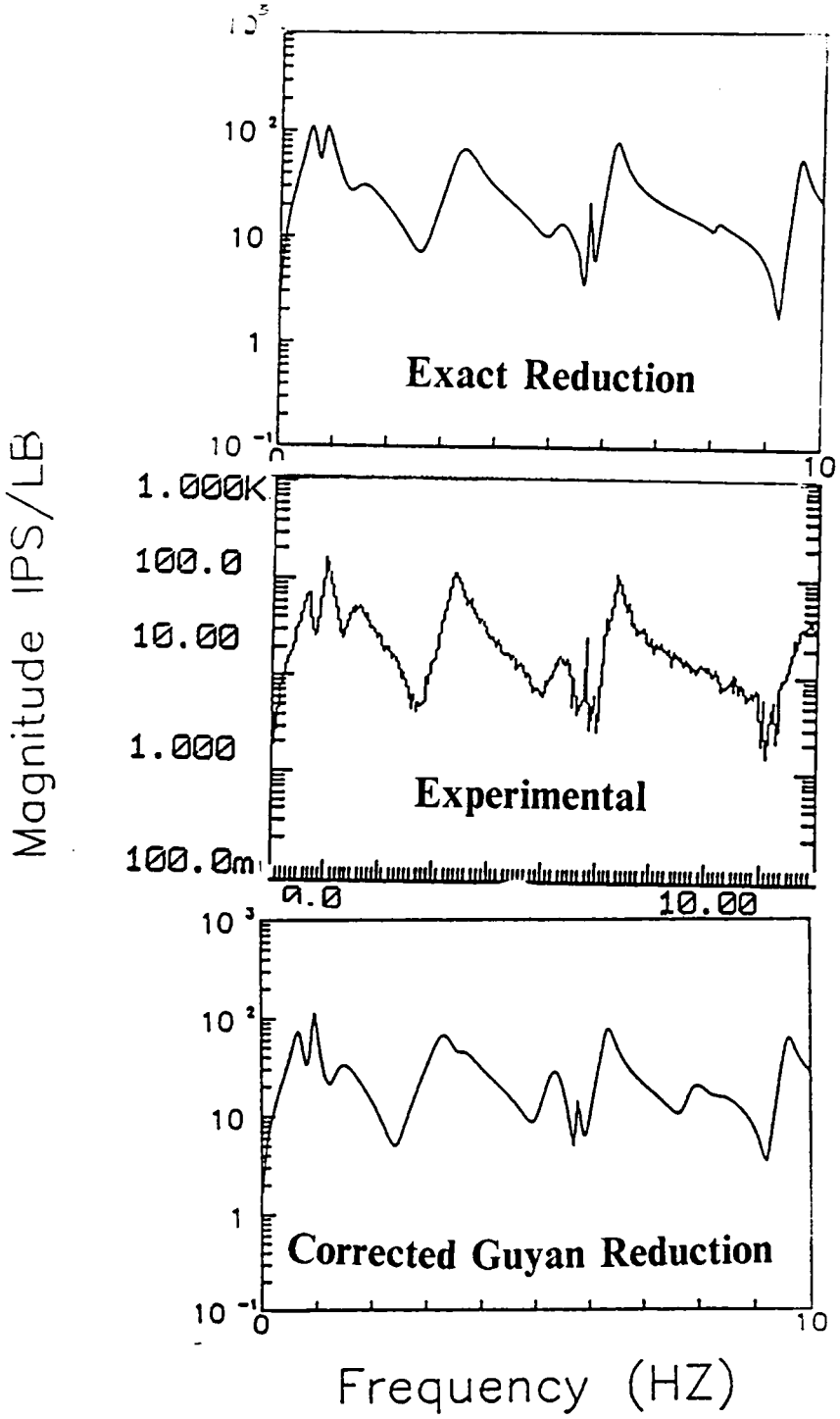

Figure 25. Hanging Grid VFRFs for LQDRF Control on (A) Exact Reduction, (B) Experiment, (C) Corrected Guyan Reduction

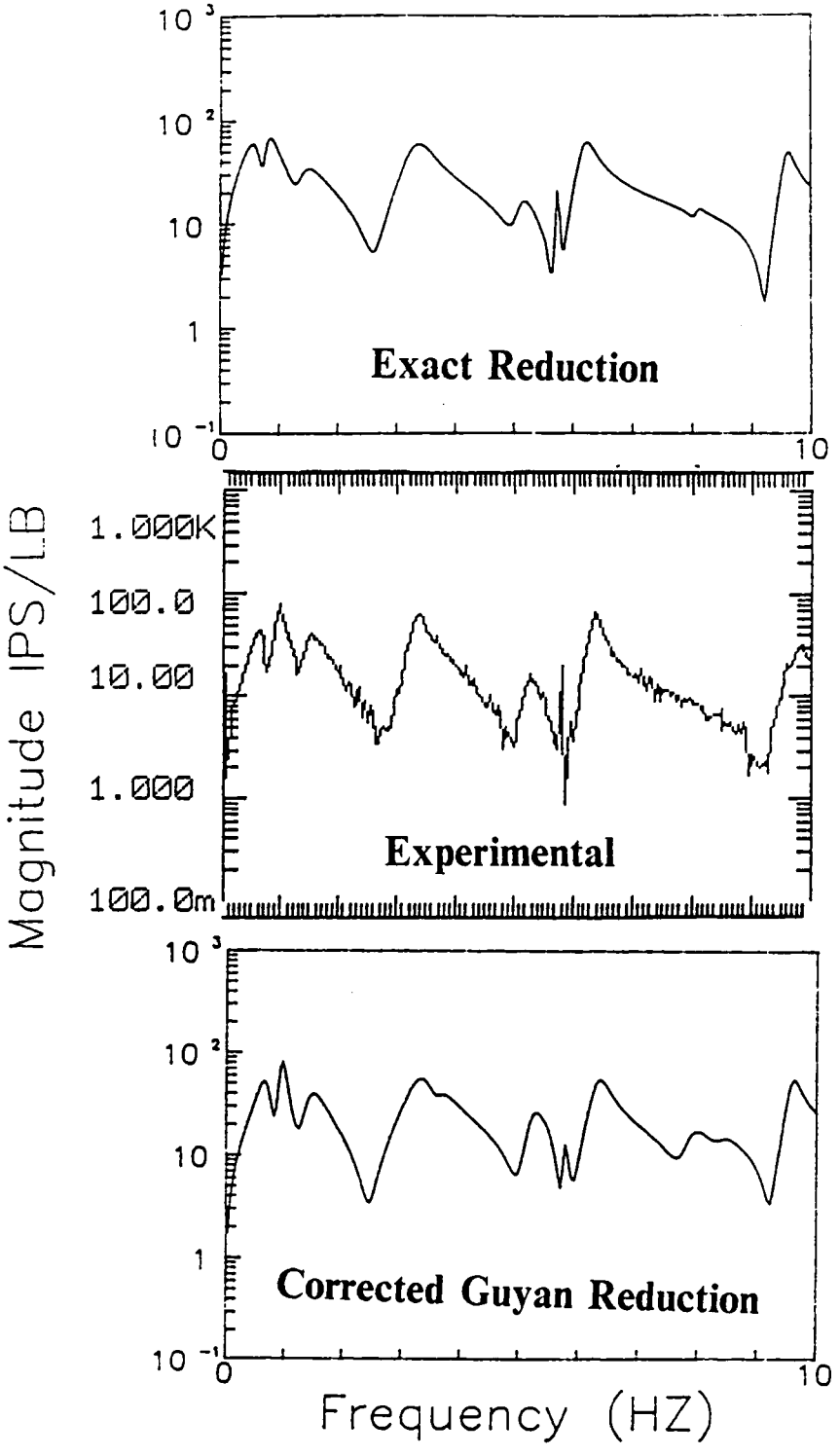

Figure 26. Hanging Grid VFRFs for Diagonal LQDRF Control on (A) Exact Reduction, (B) Experiment, (C) Corrected Guyan Reduction

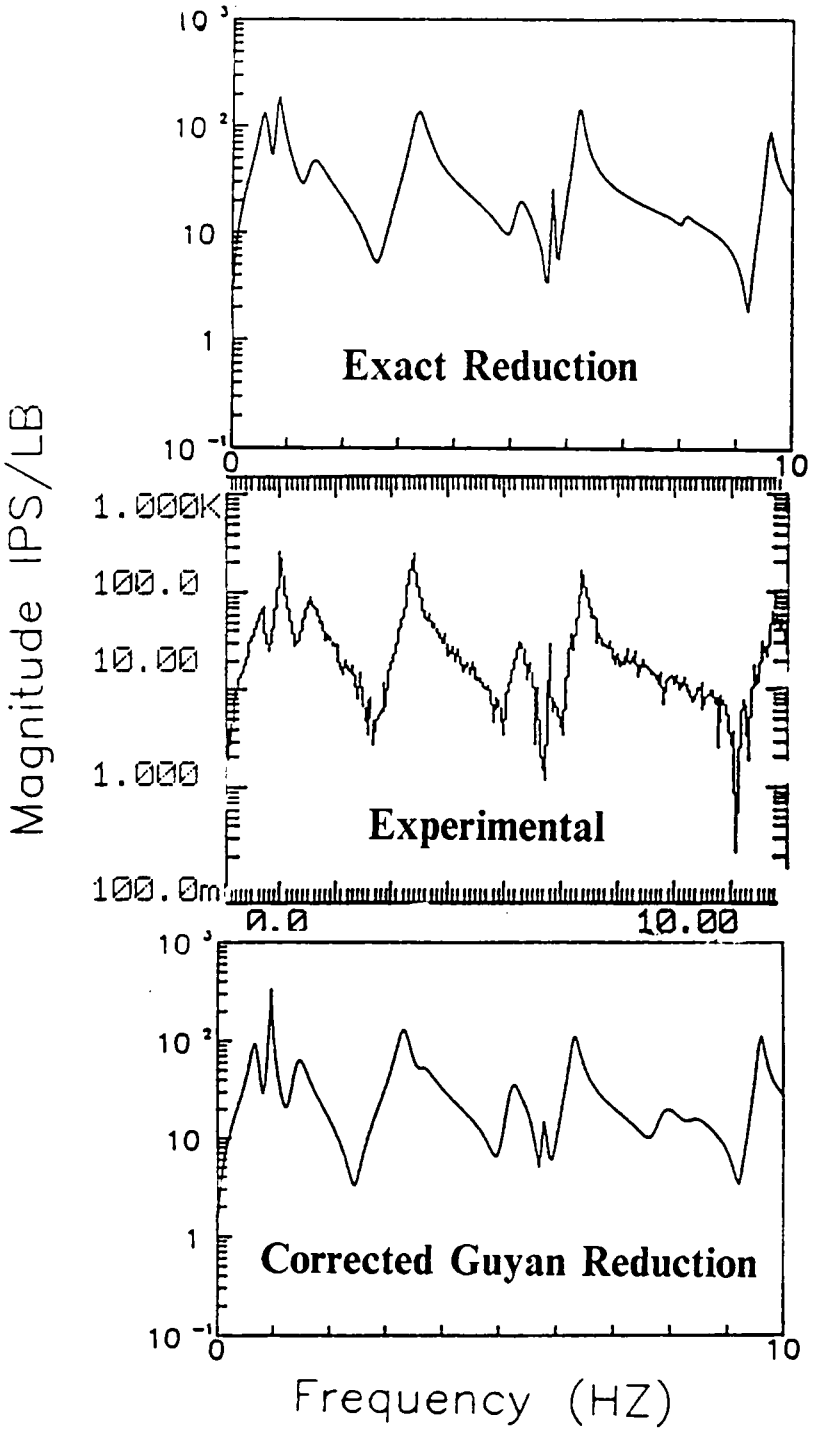

Figure 27. Hanging Grid VFRFs for LQG Control on (A) Exact Reduction, (B) Experiment, (C) Corrected Guyan Reduction

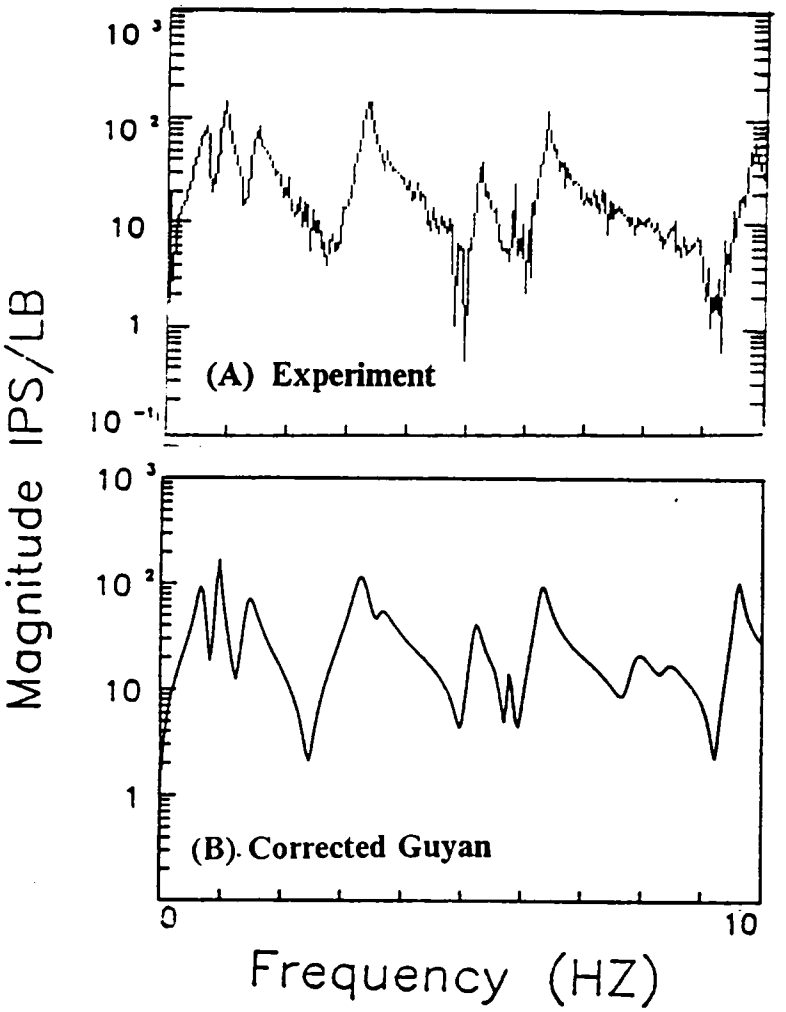

Figure 28. Hanging Grid VFRFs for MFDRF Control on (A) Experiment and (B) Corrected Guyan Reduction

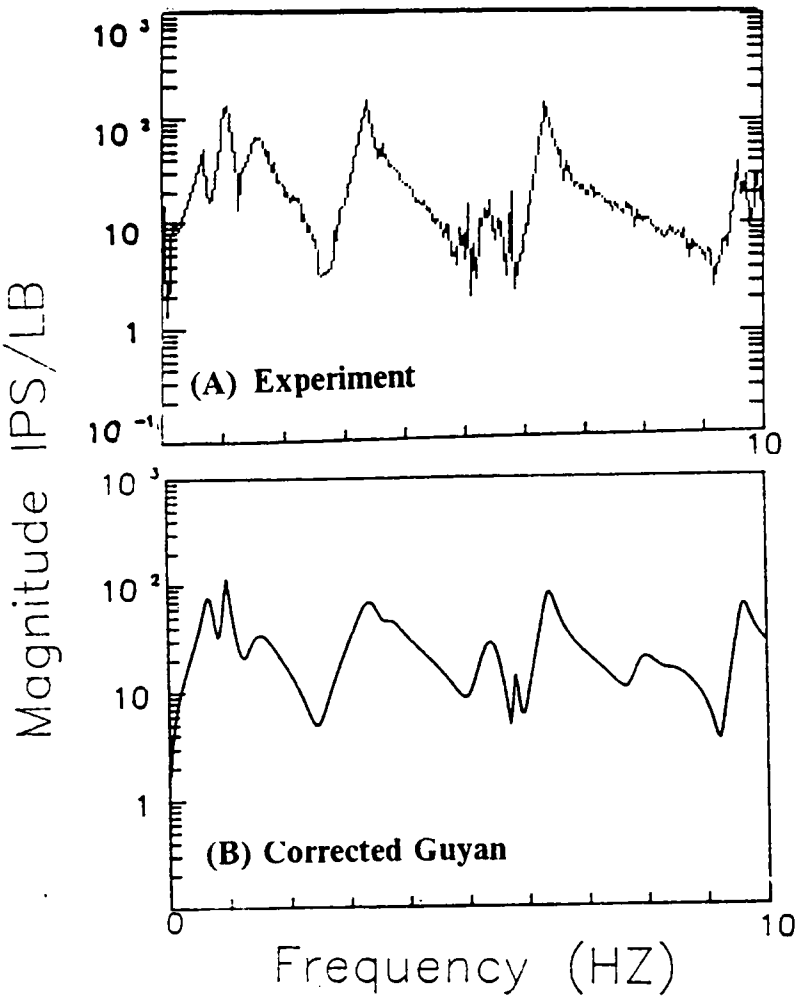

Figure 29. Hanging Grid VFRFs for LQDRF Control on (A) Experiment and (B) Corrected Guyan Reduction

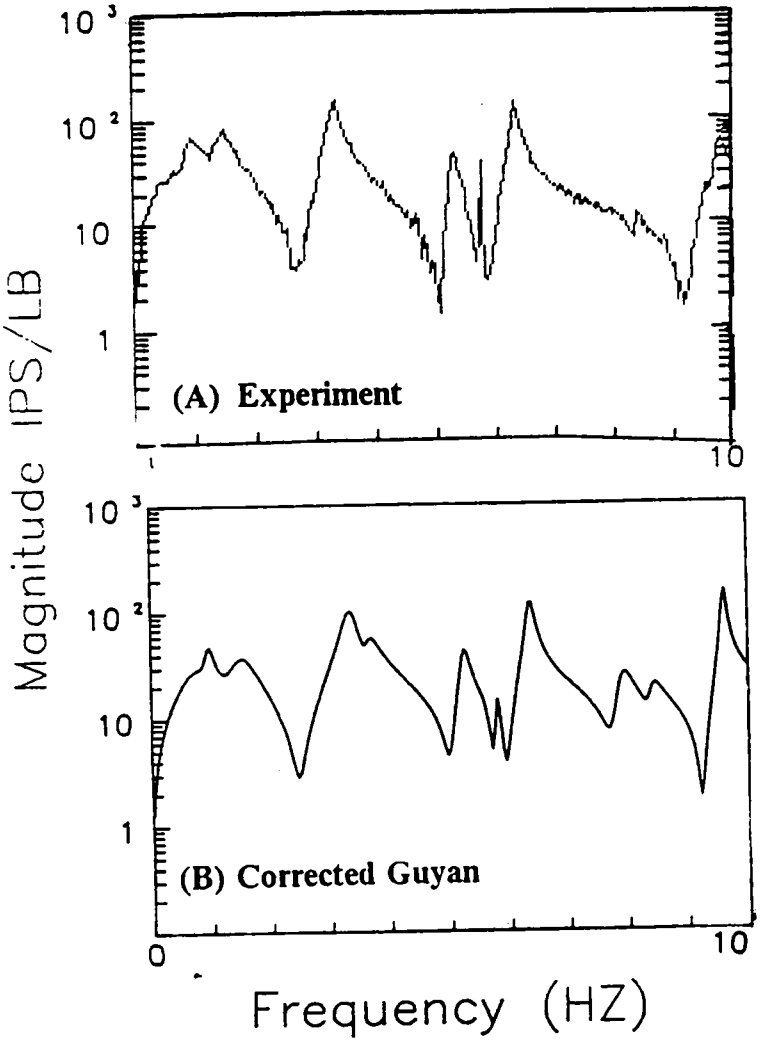

Figure 30. Hanging Grid VFRFs for diagonal LQDRF Control on (A) Experiment and (B) Corrected Guyan Reduction

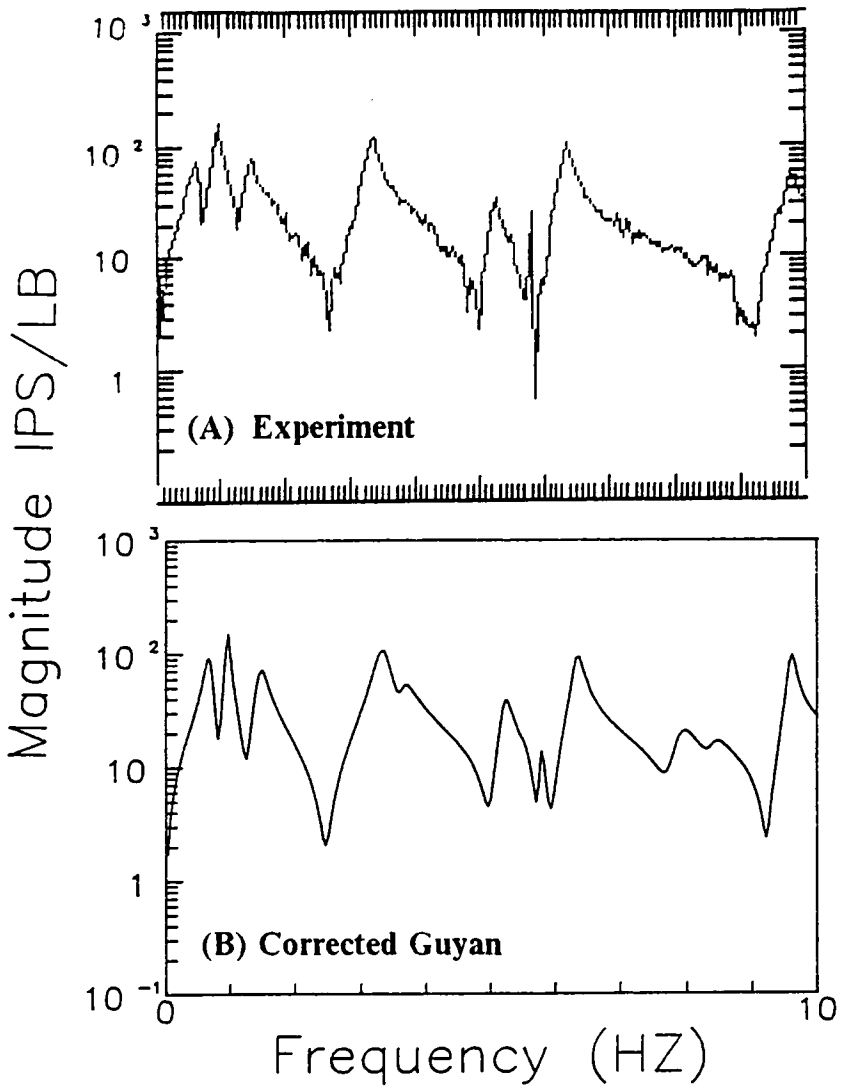

Figure 31. Hanging Grid VFRFs for LQG Control on (A) Experiment and (B) Corrected Guyan Reduction

Chapter 7

Concluding Remarks

Three types of optimized control laws were tested on two different structures, one simple - one complex. The three control laws were, a standard time-invariant linear quadratic regulator with state estimation, and two direct rate feedback control laws (one optimized for minimum force and the other optimized the linear quadratic performance index). Good agreement was found between the analytical predictions and the experimental results for the exact analytical reduction method on the simple structure without any model correction. Two model reduction methods were used on the complex structure. Both of which needed correction based on experimental measurements. The correction method used did not work well with the exact reduction method but it worked very well with the Guyan reduction method. Fair agreement between the experiment and the analysis was obtained for control systems applied to the exact reduction. This agree-

ment was improved when the control systems were applied to the corrected Guyan reduced model.

This research has demonstrated that using a model correction method based on experimental measurements improves the correlation between experimental and analytical results. Additionally, it has shown that the choice of model reduction methods affects the correction method to the point of being usable or unusable.

The implementation of control laws from the very complex LQG control law to the simple, robust diagonal DRF control law revealed that the more complex the control law the poorer the experimental/analytical correlation. The loss of performance due to using the simpler direct rate feedback control laws was shown to be only slightly more than the loss of performance due to the need for estimation when implementing the LQG control law. It was further shown that uncoupled or diagonal LQDRF control can perform as well as coupled LQDRF control with much better experimental/analytical agreement. It appears that the increasing complexity of the control systems make them more vulnerable to modelling errors in the structural model or in the modelling of the control hardware. The simpler most robust diagonal LQDRF control laws guarantee stability, are very easy to implement, provide similar performance and exhibit better correlation between experiment and analysis than the more complex LQG control law.

Chapter 8

References

[1] Guyan, R.J., "Reduction of Stiffness and Mass Matrices", AIAA Journal, Vol. 3, No. 2, Feb. 1965.

[2] Hughes, P.C., "Space Structure Vibration Modes: How Many Exist? Which Ones Are Important?," IEEE Control Systems Magazine, Vol. 7, No. 1, Feb. 1987, pp 22-28.

[3] Hughes, P.C., and Skelton, R.E., "Modal Truncation For Flexible Spacecraft," Journal of Guidance and Control, Vol. 4, No. 3, May-June, 1981, pp 241-247.

[4] Hu, A., Skelton, R.E., and Yang, T.Y., "Modeling and Control of Beam-Like Structures," Journal of Sound and Vibration, Vol. 117, No. 3, Sept. 1987, pp 475-496.

[5] Skelton, R.E., Hughes, P.C., and Hablane, H.B., "Order Reduction for Modes of Space Structures Using Modal Cost Analysis," Journal of Guidance and Control, Vol. 5, No. 4, July-Aug. 1982, pp 351-357.

[6] Perry, C.O. and Venkayya, V.B., "Issues of Order Reduction in Active Control System Design," AIAA Paper No. 86-2138, Proceedings Guidance, Navigation, and Control Conference, Aug. 18-20, 1986, Willamsburg, Va.

[7] Ramakrishnan, J.V., Rao,S.U., and Koual, L.R., "Reduced-Order Modeling of Flexible Structures," Journal of Guidance and Control, Vol. 11, No. 5, Sept.-Oct. 1988, pp 459-464.

[8] Hallauer, W.L. and Barthelemy, J.-F.M., "Active Damping of Modal Vibrations by Force Apportioning," AIAA Paper No. 80-0806, Proceedings AIAA/ASME/ASCE/AHS 21st Structures, Structural Dynamics, and Materials Conference, May 12-14, 1980, Seattle, Washington.

[9] Su, T.J. and Craig, R.R., "Model Reduction and Control of Flexible Structures Using Krylov Subspaces," AIAA Paper No. 89-1237-CP, Proceedings AIAA/ASME/ASCE/AHS/ASC 30th Structures, Structural Dynamics, and Materials Conference, April 3-5, 1989, Mobile, Alabama, pp 691-700.

[10] Kuo, C.P. and Wada, B.K., "System Identification of a Truss Type Space Structure Using the Multiple Boundary Condition Test (MBCT) Method," AIAA Paper No. 87-0746, Proceedings AIAA/ASME/ASCE/AHS 28th Structures, Structural Dynamics, and Materials Conference, Part 2A, 1987, Monterey, CA, pp 172-176.

[11] Baruch, M., and Bar-Itzhak, I.Y., "Optimal Weighted Orthogonalization of Measured Modes", AIAA Journal, Vol. 16, 1978, pp. 346-351.

[12] Baruch, M., "Optimal Correction of Mass and Stiffness Matrices Using Measured Modes", AIAA Journal, Vol. 20, 1982, pp. 1623-1626.

[13] Berman, A., "Mass Matrix Correction Using an Incomplete Set of Measured Modes," AIAA Journal, Vol. 17, 1987, pp 1147-1148.

[14] Berman, A. and Nagy, E.J., "Improvement of Large Analytical Models Using Test Data," AIAA Journal, Vol. 21, 1983, pp 1168-1173.

[15] Chen, J.C., Kuo, C.P., and Garba, J.A., "Direct Structural Parameter Identification by Modal Test Results," AIAA/ASME/ASCE/AHS 24th Structures, Structural Dynamics, and Materials Conference, Proceedings Part 2, May 1983.

[16] Dobson, B.J., "Modification of Finite Element Models Using Experimental Modal Analysis," Proceedings IMAC 2 , Feb. 1984.

[17] Hendricks, S.L., Rajaram, S., Kamat, M.P. and Junkins, J.L., "Identification of Large Flexible Structure Mass/Stiffness and Damping From On-Orbit Experiments," Journal of Guidance and Control, Vol.17, 1984, pp 224-245.

[18] Lin, C.S., "Location of Modeling Errors Using Modal Test Data," AIAA Paper No. 89-1240-CP, Proceedings AIAA/ASME/ASCE/AHS/ASC 30th Structures, Structural Dynamics, and Materials Conference, April 3-5, 1989, Mobile, Alabama.

[19] Allen, J.J. and Martinez, D.R., "Automating the Identification of Structural Model Parameters," AIAA Paper No. 89-1242-CP, Proceedings AIAA/ASME/ASCE/AHS/ASC 30th Structures, Structural Dynamics, and Materials Conference, April 3-5, 1989, Mobile, Alabama.

[20] Pappa, R.S. and Juang, J.-N., "Some Experiences with the Eigensystem Realization Algorithm," Proc. of the 6th International Modal Analysis Conference, Vol. II, 1988, pp 1575-1581, also Sound and Vibration, Vol. 22, No. 1, Jan. 1988, pp 30-34.

[21] Yurkovich, S., "System Identification Experiments for Flexible Structure Control," Dynamics and Control of Large Structures, Proc. of 6th VPI&SU/AIAA Symposium, Blacksburg, VA, ed. by L. Meirovitch, 1987, pp 143-157.

[22] Schafer, B. and Holzach, H., "Identification and Model Adjustment of a Hanging Plate Designed for Structural Control," Proc. of 2nd International Symposium on Structural Control, Waterloo, Ont., Canada, ed. by H.H.E. Leipholz, Martinus Nijhoff Publishers, 1987, pp 631-650.

[23] Das, A.M Strange, T.J., Schlaegel, W.T. and Ward, J.M., "Experiments in Modeling and Parameter Estimatin of Flexible Structures," NASA/DOD Control/Structures Interaction Technology Meeting, 1987, AFWAL-TR-88-3052, 1988, pp 389-400.

[24] Nurre, G.S., Ryan, R.S., Scofield, H.N., and Sims, J.L., "Dynamics and Control of Large Space Structures," Journal of Guidance, Control, and Dynamics, Vol. 7, No. 5, Sept.-Oct. 1984, pp 514-526.

[25] Aubrun, J.N., Rainer, M.J., and Lyons, M.G., "Structural Control for a Circular Plate," Journal of Guidance, Control and Dynamics, Vol. 7, No. 5, Sept.-Oct. 1984, pp 514-526.

[26] Schaechter, D.B. and Eldred, D.B., "Experimental Demonstration of the Control of Flexible Structures," Journal of Guidance, Control, and Dynamics, Vol. 7, No. 5, Sept.-Oct. 1984, pp 535-545.

[27] Bauldry, R.D., Breakwell, J.A., Chambers, G.J., Johnson, K.F., Nguyen, N.C., and Schaechter, D.B., "A Hardware Demonstration of Control for a Flexible Offset-Feed Antenna," The Journal of Astronautical Sciences, Vol. 31, No. 3, July-Sept. 1983, pp 437-442.

[28] Skidmore, G.R. and Hallauer, W.L., "Modal-Space Active Damping of a Beam-Cable Structure: Theory and Experiment," Journal of Sound and Vibration, Vol. 101, No. 2, July 1985, pp 149-160.

[29] Hallauer, W.L., Skidmore, G.R., and Gehling, R.N., "Modal-Space Active Damping of a Plane Grid Structure: Theory and Experiment," Journal of Guidance, Control, and Dynamics, Vol. 8, No. 3, May-June 1985, pp 366-373.

[30] Skidmore, G.R. and Hallauer, W.L., "Experimental-Theoretical Study of Active Damping with Dual Sensors and Actuators," AIAA Paper No. 85-1921, Proceedings AIAA Guidance, Navigation, and Control Conference, 1985, pp 433-442.

[31] Balas, G.J., Lukich, M., Dailey, R.L. and Doyle, J.C., "Robust Control of a Truss Experiment," AIAA Paper No. 88-4084, Proceedings AIAA Guidance, Navigation and Control Conference, Part 1, 1988, pp 245-252.

[32] Lukich, M., "System Identification & Control of the Truss Experiment: A Retrospective," AIAA Paper No. 88-4084, Proceedings AIAA Guidance, Navigation and Control Conference, Part 2, 1988, pp 821-831.

[33] Dailey, R.L. and Lukich, M., "Recent Results in Identification and Control of a Flexible Truss Structure," Proc. of the 1988 American Control Conference, Vol. 2, 1988, pp 1468-1473.

[34] Martinovic, Z.N., Schamel, G.C., Haftka, R.T., and Hallauer,W.L.,Jr., "An Analytical and Experimental Investigation of Output Feedback vs. Linear Quadratic Regulator," Scheduled for publication in July/August 1989 issue of Journal of Guidance, Control, and Dynamics.

[35] Haftka, R.T., Martinovic, Z.N., and Hallauer, W.L.,Jr., "Enhanced Vibration Controllability by Minor Structural Modification," AIAA Journal, Vol. 23, Aug. 1985, pp 1260-1266.

[36] Haftka, R.T., Martinovic, Z.N., Hallauer, W.L.,Jr., and Schamel,G.C., "An Analytical and Experimental Study of Control System Sensitivity to Structural Modifications," AIAA Journal, Vol. 25, Feb. 1987, pp. 310-315.

[37] Schamel, G.C., and Haftka, R.T., "LQG and Direct Rate Feedback Control with Model Reduction on a Flexible Laboratory Grid Structure," Dynamics and Control of Large Structures, Proc. of the 7th VPI&SU Symposium, Blacksburg, VA, ed. by L. Meirovitch, May 8-10, 1989.

[38] Schafer, B.E. and Lange, T., "Dynamic and Control Experiments on Large Space Structures at DFVLR," Control-Theory and Advanced Technology, Vol. 4, No. 1, March 1988, pp 673-680.

[39] Greeley, S.W., Phillips, D.J. and Hyland, D.C., "Experimental Demonstration of the Maximum Entropy/Optimal Projection Design Theory for Active Vibration Control," Proc. of the 1988 American Control Conference, Vol. 2, 1988, pp 1462-1467.

[40] Joshi, S.P., Vincent, T.L., and Lin, Y.C. "Control for Energy Dissipation in Structures," AIAA Paper No. 88-2272, Proceedings AIAA/ASME /ASCE/AHS/ASC 29th Structures, Structural Dyanmics and Materials Conference, Willamsburg, Virginia, April 16-18, 1988, Part 1, pp 479-490.

[41] Hallauer, W.L., and Wagie, D.A., "An Inexpensive Experiment for Undergraduates an Active Control of Structural Vibrations," 1989 ASEE Annual Conference Proceedings, 1989.

[42] Natori, M., Motohashi, S., Takahara, K. and Kuwao, F., "Vibration Control of Truss Beam Structures using Axial Force Actuators," AIAA Paper No. 88-2273, 29th Structures, Structural Dynamics, and Materials Conference, Williamsburg, Virginia, April 16-18, Part 1, 1988, pp 491-499.

[43] Robertshaw, H.H., Wynn, R.H., Kung, H.F., Hendricks, S.L., and Clark, W.W., "Dyanmics and Control of a Spatial Active Truss Actuator," AIAA Paper No. 89-1328, AIAA/ASME/ASCE/AHS/ASC 30th Structures, Structural Dynamics, and Materials Conference, Mobile, Ala, April 3-5, 1989, Part 3, pp 1473-1479.

[44] Miller, D.W. and Crawley, E.F., "Theoretical and Experimental Investigation of Space-Realizable Inertial Actuation for Passive and Active Structural Control," Journal of Guidance, Control and Dynamics, Vol. 11, No. 5, Sept.-Oct. 1988, pp 449-458.

[45] Zimmerman, D.C. and Inman, D.J., "Practical Implementation Issues Active Control of Large Flexible Structures," Dynamics and Control of Large Struc-

tures, Proc. of the 6th VPI&SU Symposium, Blacksburg, VA, ed. by L. Meirovitch, 1987, pp 275-290.

[46] Hallauer, W.L. and Lamberson, S.E., "Experimental Active Vibration Damping of a Plane Truss Using Hybrid Actuation," AIAA Paper No. 89-1169, AIAA/ASME/ASCE/AHS/ASC 30th Structures, Structural Dynamics and Materials Conference, Mobile, Ala, April 3-5,1989, Part 1, pp 80-90.

[47] Ghosh, D., Montgomery, R.C., Norris, M. and Meirovitch, L., "Linear Estimation and Control Studies of Vibration of the SCOLE Flexible Mast," Dynamics and Control of Large Structures, Proc. of the 7th VPI&SU Symposium, Blacksburg, VA, May, 8-10, 1989, ed. by L. Meirovitch, 1989.

[48] Rahman, Z., Junkins, J., Pollock, T. and Bang, H., "Large Angle Maneuvers with Vibration Suppression: Analytical and Experimental Results," Dynamics and Control of Large Structures, Blacksburg, VA, May 8-10, 1989, Proc. of the 7th VPI&SU/AIAA Symposium, ed. by L. Meirovitch, 1989.

[49] Schamel, G.C., "Active Damping of a Structure with Low Frequency and Closely Spaced Modes: Experiments and Theory," M.S. Thesis, VPI&SU, March, 1985.

[50] Martinovic, Z. N., Haftka, R. T., Hallauer, W. L. Jr., and Schamel, G. C. II, "A Comparison of Active Vibration Control Techniques: Output Feedback Vs. Optimal Control", AIAA Paper 87-0904-CP, AIAA Dynamics Specialists Conference, Monterey CA, April 1987, Part 2b pp.610-621.

[51] Masse, M.A., "A Plane Grillage Model for Structural Dynamics Experiments: Design, Theoretical Analysis and Experimental Testing," M.S. Thesis, VPI&SU, 1983.

[52] Gehling, R.N., "Experimental and Theoretical Analysis of a Plane Grillage Structure With High Modal Density," M.S. Thesis, VPI&SU, 1984.

[53] Craig, R.R. Jr., Structural Dynamics, An Introduction to Computer Methods, John Wiley & Sons, 1981, pp.383-389

[54] Argyris, J.H., Hilpert, O., Malejannekis, G.A., and Scharpf, D.W., "On the Geometrical Stiffness of a Beam in Space--A Consistent V.W. Approach," Computer Methods in Applied Mechanics and Engineering, Vol. 20, 1979, pp 105-131.

[55] Hallauer, W.L. and Trivedi, D.J., "An Experimental Study of Transient Waves in a Plane Grid Structure," AIAA Journal, Vol. 26, No. 2, Feb 1988, pp 228-234.

[56] Kwakernaak, H., and Sivan, R., Linear Optimal Control Systems, Wiley, 1972.

[57] Anderson, B.D.O., and Moore, J.B.,Linear Optimal Control, Prentice-Hall,Inc., 1971. p. 50.

[58] Kammer, D. C., and Sesak, J. R., "Actuator Number Versus Parameter Sensitivity in Flexible Spacecraft Control", Proceedings of Second VPI & SU/AIAA Symposium on Dynamics and Control of Large Flexible Spacecraft, Blacksburg, Va., 1979, pp. 421-441.

[59] Martinovic, Z.N., "Sensitivity of Active Vibration Control to Structural Changes and Model Reduction," Ph.D. Dissertation, VPI&SU, Blacksburg, Va, May 1987.

[60] Joshi, S. M., "Robustness Properties of Collocated Controllers for Flexible Spacecraft," Journal of Guidance, Control, and Dynamics, Vol. 9, No. 1, January-February, 1986, pp. 85-91.

[61] Thareja, R., and Haftka, R.T., "NEWSUMT-A, A General Purpose Program for Constrained Optimization Using Constraint Approximations," ASME

Journal of Mechanics, Transmission, and Automation in Design, March 1985, pp. 94-99.

[62] Skidmore, G.R., "A Study of Modal-Space Control of a Beam-Cable Structure: Experiments and Theory," M.S. Thesis, VPI&SU, 1983.

[63] Skidmore, G.R., "Experimental-Theoretical Study of Velocity Feedback Damping of Structural Vibrations," Ph.D. Dissertation, VPI&SU, 1985.

[64] Travassos, R.H., "The MCP-100: A Turnkey System for Implementing Multivariable Output Feedback Flight Control Laws," National Aerospace and Electronics Conference, May 1982.

[65] Franklin, G.F., and Powell, J.D., Digital Control of Dynamic Systems, Addison-Wesley Publishing Company, Inc., Philippines, 1980, p.31.

Appendix A

Nomenclature

A	state space system matrix
B	state space control selection matrix
C	state space output selection matrix
c	inherent damping matrix
D	active damping matrix ($n_c x n_c$)
e	state reconstruction error vector ($2nx1$)
F	state feedback matrix
$\mathbf{F}_D$	gain matrix ($n_c x 2n$)
FIJ	matrix partitions
f_i	maximum force ratio
f_c	corner frequency of low-pass filter
g_j	j-th constraint in optimization problems
K	optimal state estimation matrix

$\mathbf{k}$	structural stiffness matrix
$\mathbf{I}$	identity matrix of appropriate order
$\mathbf{J}$	quadratic performance index
$\mathbf{m}$	mass matrix
M_i	i-th modal mass, i = 1,..., n_R
n	number of degrees of freedom
n_c	number of control actuators
n_f	number of initial conditions
n_m	number of stability margin constraints
n_R	number of degrees of freedom of reduced model
n_s	number of sensors
$\mathbf{Q}$	state weighting matrix
$\mathbf{q}$	vector of physical displacements ($nx1$)
$\dot{q}_j$	velocity measured by j-th sensor, j = 1,..., n_s
$\mathbf{R}$	control weighting matrix
$\mathbf{S}$	Riccati solution matrix for regulator design
$\mathbf{S}_f$	Riccati solution matrix for filter design
$\mathbf{U}$	applied load distribution matrix (nxn_c)
$\mathbf{u}$	control input vector ($n_c x1$)
$\mathbf{w}_1$	vector of state excitation noise ($2nx1$)
$\mathbf{w}_2$	vector of state measurement noise ($2nx1$)
$\mathbf{V}_1$	state excitation noise covariance matrices
$\mathbf{V}_2$	state measurement noise covariance matrices

$\mathbf{x}$	state vector of structural motion ($2nx1$)
$\mathbf{y}$	sensor output vector
α	prescribed stability margin for filter poles
β	performance index for LQDRF control
γ	performance index for MFDRF control
ζ	damping ratio
Φ	modal matrix (nxn)
ϕ_i	open loop modal vector of mode i
ω_i	i-th natural frequency
$\mathbf{0}$	zero matrix of appropriate order

Overbars and Subscripts

$\hat{()}$	corrected reduced system
$\overline{()}$	augmented system
$\tilde{()}$	closed loop system
$()_{est}$	estimated state
$()_{Part}$	Partitioned matrix
$()_R$	reduced model
$()_E$	augmented reconstructed matrix
$()_0$	initial value
$()_L$	lower limit

The vita has been removed from the scanned document